

Linköping University | Department of Physics, Chemistry and Biology
Master Thesis, 30 hp | Applied Physics and Electrical Engineering
Spring term 2022 | LITH-IFM-A-EX—20/3823-SE

Modeling of optical microresonator frequency combs

Michael Ekström

Examiner, Prof. Magnus Johansson
Tutor, Dr. Tobias Hansson



Abstract

An optical frequency comb is a structure of equidistant, coherent spectral components which can be thought of as a large array of individual phase-locked laser sources. Their utilization in precision spectroscopy garnering part of the 2005 Nobel prize, optical frequency combs constitute a relatively novel technology with a large number of potential and actual applications. The research interest grew further with the 2007 discovery of comb structures in microresonators enclosing a nonlinear Kerr medium pumped by an external continuous wave laser, offering both substantially wider combs and the prospect of chip-scale integration.

In this thesis work, the modeling of frequency comb spectra generated through optical Kerr cavities is considered using both an Ikeda map and the mean-field Lugiato-Lefever equation to describe the intracavity field evolution. Derivations of these mathematical models are first reviewed alongside relevant physics. They are then treated analytically to constrain model parameters to regions of interest in the context of Kerr-comb dynamics. Finally, numerical parameter sweeps are conducted in both models with respect to the pump power and frequency detuning, where the Ikeda map is additionally examined in the high-energy regime not faithfully described by the Lugiato-Lefever equation.

The produced phase diagrams reveal a complex landscape of dynamics including Turing patterns, temporal cavity solitons, breathers and chaos. Ikeda map parameters in the high-energy regime capable of supporting previously reported super energetic cavity solitons are also investigated. Lastly, the numerical simulation package developed for parameter sweeps is presented.

Acknowledgements

I would like to express my deepest gratitude to Dr. Tobias Hansson, not only for offering the chance to work on a fascinating thesis project, but also for his inexhaustible patience in answering questions and accommodating the shifting working conditions encountered. I am also grateful to Prof. Magnus Johansson for his insightful comments and general support during the project, in addition to sparking my original interest in nonlinear phenomena.

Contents

1	Introduction	1
1.1	Optical frequency combs	1
1.2	Kerr combs	2
1.2.1	Four-wave mixing	3
1.2.2	Multistability	3
1.2.3	Dynamical regimes	5
1.2.4	Mathematical models	6
1.3	Problem	7
1.3.1	Goals	7
1.3.2	Methods	7
1.3.3	Delimitations	7
1.4	Thesis structure	8
2	The Ikeda map	9
2.1	Pulse propagation	9
2.1.1	Attenuation	13
2.1.2	Nonlinearity	14
2.1.3	Propagation equation	16
2.2	Boundary condition	18
2.2.1	Critical coupling	19
2.3	Parameter reduction	20
3	Lugiato-Lefever equation	22
4	Analytical methods	24
4.1	Bistability	24
4.2	Multistability	25
4.3	Modulational instability	26
5	Numerical methods	28
5.1	Operator splitting	29
5.2	Split-step Fourier method	29
5.2.1	Ikeda map	30
5.2.2	Lugiato-Lefever equation	31
6	Software design and simulations	32
6.1	Design process and goals	32
6.2	Kerr comb simulation application	34
6.3	System and simulation parameters	34
6.4	Workflow	36

7	Results and discussion	37
7.1	Low-power region	37
7.2	High-power region	40
7.3	Validity of results	42
8	Conclusions	43
A	Ikeda map code	44
B	Lugiato-Lefever equation code	46
C	Simulation data	48

Chapter 1

Introduction

This chapter outlines the background, purpose and structure of the thesis. First, the general theory of frequency combs and a few examples of their applications is briefly surveyed. Particular emphasis is placed on Kerr frequency combs and their wide array of dynamics relevant to comb formation, along with mathematical models used to describe them. Next, the goals, methods and delimitations of the work are established. Finally, the structure of the remaining document is described.

1.1 Optical frequency combs

Optical frequency combs are structures of equally spaced spectral components spanning a wide band of frequencies. If the components, or comb teeth, are additionally phase-locked, the time domain representation takes the form of a pulse train (figure 1.1). Their utilization in precision spectroscopy garnering part of the 2005 Nobel prize, optical frequency combs constitute a relatively novel technology with a large number of potential and actual applications.

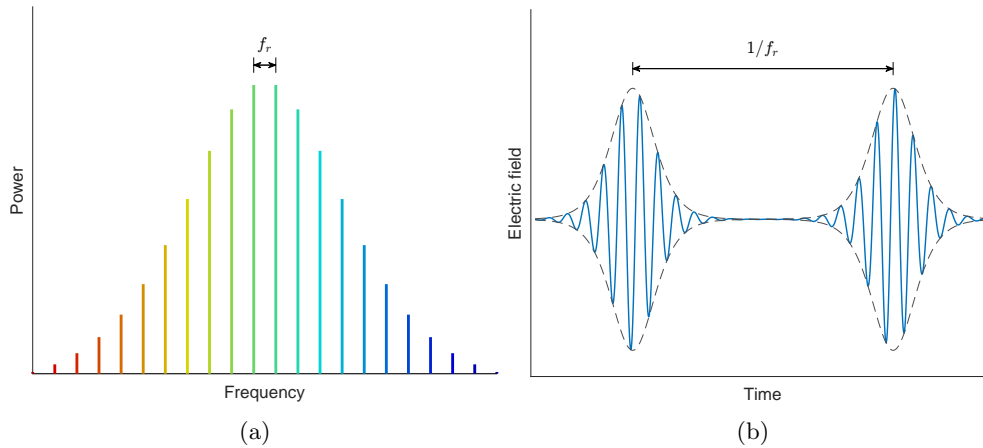


Figure 1.1: Frequency domain (a) and time domain (b) sketch of a phased-locked frequency comb. Note that the pulsed temporal behavior is only observed for combs with phase correlated spectral components.

Beyond spectroscopy, these include optical clocks with the ability to count cycles of light [1], terabit wavelength-division multiplexing using a wide array of coherent frequency channels generated by a single laser [2], and calibration of astrophysical spectrometers to resolve the minute Doppler shifts associated with stars orbited by exoplanets [3], to name a few. A common analogy used to illustrate their usefulness is that of the light gear [4]: assuming phase-locked

comb teeth, an external source can be locked or "engaged" to a tooth at one end of the comb, and an equivalent but frequency shifted representation can be extracted at the other. If the comb is broad enough, this permits reading of individual optical cycles in the microwave range, or, conversely, optical waveform synthesis using microwaves. Another useful analogy is a light ruler [5], enabling frequency domain measurements by reading the beating produced by the interference of a signal and individual comb teeth.

Once a phase-locked comb structure has been generated, the absolute distance between spectral components is easy to ascertain as the inverse time between emitted pulses or repetition rate f_r . In other words, the comb teeth are spaced in multiples of the cavity free spectral range (FSR). The frequency of tooth n is then known up to a carrier envelope offset f_0 through

$$f_n = f_0 + n f_r. \quad (1.1)$$

The offset f_0 is responsible for a mismatch between the electric field and pulse periodicity, causing each pulse to not be identical. For the comb to become truly useful in many applications, this offset must be determined. To this end, a special class of combs which span an entire octave or more is especially useful, since a tooth from one side can then be frequency doubled and referenced with one twice its original frequency¹. This process, known as self-referencing, allows f_0 to be determined and even eliminated using feedback control [6]. The conclusion is that broad combs spanning wide bands of frequencies are desirable.

1.2 Kerr combs

The key component to the realization of frequency combs is nonlinear effects, since a linear optical system offers no mechanism for new frequencies to be generated. The original success in generating frequency combs came with mode-locked lasers using a saturable absorption non-linearity [4]. The time domain interpretation of its operation can be described in terms of the intensity dependent damping of an optical pulse traversing the laser cavity, where the fringes are attenuated more than the peak. This results in a narrowing of the pulse which acts in opposition to the dispersion-induced broadening. Provided appropriate laser pumping to compensate for the energy transmitted out of the resonator, this process can converge to produce a circulating solitary pulse, or soliton, of constant shape, corresponding to a phase-locked comb in the frequency domain.

A more recent development, however, was the realization of frequency combs in microresonators using the nonlinear Kerr effect [7], that is, an intensity dependent refractive index

$$n = n_0 + n_2 I, \quad (1.2)$$

where the optical intensity I induces a change in the linear refractive index n_0 proportional to the Kerr coefficient n_2 . These resonators generally trap light using whispering-gallery modes in circular dielectric structures [8] and can sport high Q values (the average lifetime of circulating photons times frequency) in addition to small mode volumes, which increases the intensity and therefore the nonlinearity. Unlike mode-locked lasers, Kerr-based frequency combs are passive in the sense that no population inversion occurs and an external continuous wave (CW) laser source is instead used to pump the cavity, further reinforcing the gearbox analogy. First demonstrated experimentally in 2007, this approach has a number of attractive features. Perhaps the most obvious advantage is the prospect of widespread deployment owing to the small scale and low power consumption of the resonator, along with the potential for chip-scale integration. Another benefit is high repetition rates, which in the frequency domain translates to a broader comb.

¹It is also possible to self-reference combs of lower frequency spans, e.g. 2/3 of an octave by doubling the higher end and tripling the lower.

1.2.1 Four-wave mixing

The operating principle behind Kerr combs is parametric² frequency conversion through four-wave mixing (FWM) enabled by the third order susceptibility $\chi^{(3)}$ of the medium [4]. This phenomenon involves the instantaneous annihilation of two cavity photons followed by the creation of two new ones, constrained by energy and momentum conservation. The process is initially fueled by pump photons, then referred to as degenerate FWM since the annihilated photons are of equal frequency ω_p , and the two resulting photons of frequency ω_+ , ω_- are equally spaced relative to the pump frequency due to energy conservation $2\hbar\omega_p = \hbar\omega_+ + \hbar\omega_-$. Most of the photons produced this way are short-lived, but a few land in adjacent cavity resonances and are able to persist longer. It is then possible for spectral sidebands to start growing symmetrically around the pump frequency and for the initially homogeneous field envelope to develop a periodic modulation. The parametric sideband amplification only happens if the number of photons entering the modes exceeds the number leaving (either from attenuation or coupling), and is therefore typically associated with a threshold value of the intracavity power. This nonlinear phenomenon called modulational instability (MI) [10][11] is well understood and extensively studied in weakly nonlinear optical fibers over long distances [12][13].

If the sidebands grow large enough, non-degenerate or cascaded FWM starts to take over as photons of different frequencies ω_1 and ω_2 separated by $\Delta = \omega_2 - \omega_1$ interact and produce new pairs at $\omega_+ = \omega_2 \pm \Delta$ and $\omega_- = \omega_1 \mp \Delta$ which crucially adhere to the comb spacing structure. As new photons are produced at frequencies farther and farther away from the initial pump and sideband modes, however, they become increasingly misaligned with the dispersion shifted cavity modes, which is the main limiting factor in broadening the comb spectrum.

While the immediate two neighbors of the pump mode are the main recipients of photons produced by the initial degenerate FWM, some also enter more distant modes. If the parametric sideband amplification is activated for these modes as well, several cascaded FWM comb formations, referred to as subcombs, can occur in parallel to the main comb. Since the modes that originated the subcombs are slightly shifted from the main comb spacing due to dispersion, this results in several densely packed spectral components in each tooth and a low-quality comb. This was identified as the main source of noise in initial attempts at creating Kerr combs [4], later resolved by the discovery of temporal cavity solitons, discussed later.

1.2.2 Multistability

Another important manifestation of the nonlinear Kerr effect is the change in optical path length induced by the optical power, called self-phase modulation [13]. At low intensity, the cavity responds similarly to a linear system when the pump frequency is varied or detuned from resonance, where the intracavity power follows a Lorentzian curve with maximum at zero (figure 1.2). When higher intracavity powers are involved, however, the resonant frequency shifts due to the different refractive index and resulting optical path length experienced by the circulating field. As the cavity power grows approaching resonance, the resonant frequency is then increasingly shifted away from zero detuning $\delta = 0$, resulting in an overall tilt of the curve. With enough tilt, the resonance curve starts to overlap with itself and gains a section with three possible CW solutions of different amplitude for a single value of detuning, the outer two of which are stable with respect to homogeneous perturbations [14]. The system is then said to be bistable.

Which solution ends up existing inside the cavity for bistable regions depends on the detuning history. If scanned from negative values (corresponding to higher pump frequencies) towards positive, the cavity power follows the upper branch until the shifted resonance peak is reached. It then falls to the lower branch where it stays until the detuning is scanned back beyond the branch start at which point it jumps back to the upper one, tracing a hysteresis cycle. The

²In the context of photonics, a parametric process is one that does not involve changing the population of the medium through photon absorption and is conservative [9].

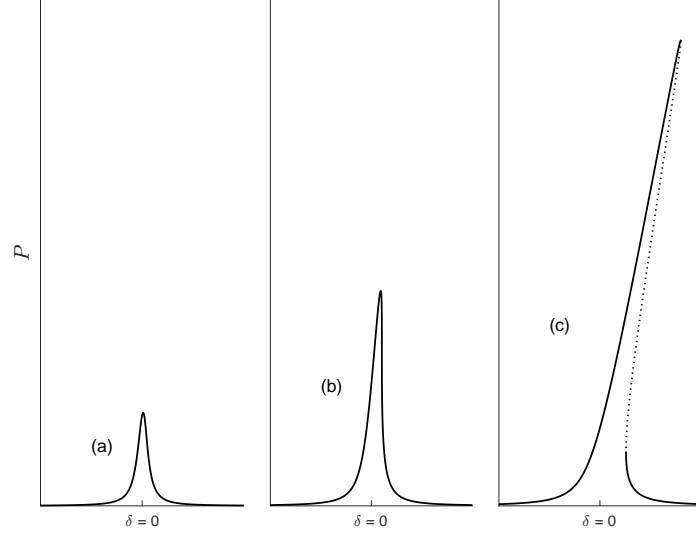


Figure 1.2: The intracavity power P as a function of pump frequency detuning δ for increasing pump values. For low powers, the relationship is close to a Lorentzian curve (a). With higher pump power, the curve develops a tilt (b), and with enough tilt the curve gains a region with bistability (c). The unstable middle branch is marked by a dotted line.

bistable behavior is interesting for several potential applications, but in the context of Kerr frequency combs its significance lies in the realization that bistable regions in resonators can support localized, bright temporal cavity solitons which propagate as a brief coupling of the modulationally stable lower branch to the upper one [15].

At high enough cavity power, the peaks of adjacent mode resonances can start to overlap each other, forming regions with more than two simultaneous solutions referred to as multistability (figure 1.3). It was predicted [16] and later experimentally confirmed [17] that these regions can support solitons of significantly higher peak intensity and shorter temporal widths than those associated with bistable regions. They are therefore interesting for Kerr frequency comb development since this yields a broader comb compared to those produced by ordinary cavity solitons.

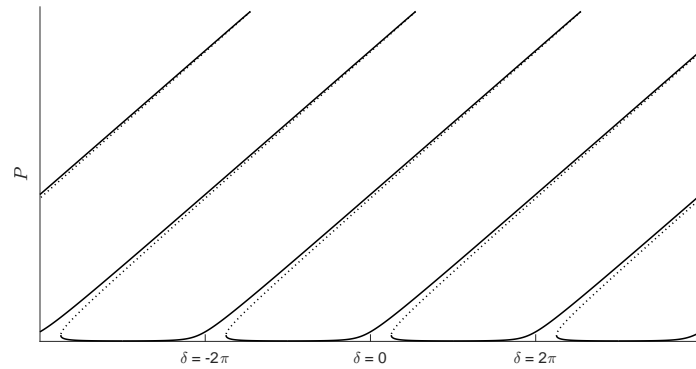


Figure 1.3: Intracavity power P for different pump frequency detuning δ and constant pump power. Multistable regions appear beyond the bistability range with overlapping adjacent mode resonances.

1.2.3 Dynamical regimes

A diverse range of possible cavity dynamics are accessible depending on the parameter values of the system. These mainly include the intrinsic absorption α_i , group-velocity dispersion β_2 and Kerr coefficient n_2 of the medium at the pump frequency ω_0 , in addition to the pump coupling transmission coefficient θ , pump power $|E_{\text{in}}|^2$ and pump detuning δ . The group-velocity dispersion sign near the pump frequency plays an especially important role, since a negative sign (where high frequency components propagate faster than low ones), referred to as anomalous dispersion, is known to be commensurate with bright cavity solitons. A positive sign, known as normal dispersion, is also known to support dark cavity solitons where the upper branch briefly couples to the lower one, creating a propagating "dip" or hole [18].

The most easily accessible parameters to vary in a real system are the power and detuning of the pump field, and it is therefore interesting to determine what dynamical regimes can be reached through this two-dimensional parameter space, all other values being fixed. As it turns out, all relevant dynamics with respect to frequency comb formation can be observed by moving, or sweeping, through appropriate values of power and detuning, provided some assumptions about the other parameters, described in chapter 2. This is particularly useful from a practical standpoint, since arbitrary cavity dynamics can then in theory be excited from an empty, or cold, cavity simply by steering the pump parameters through a fixed path.

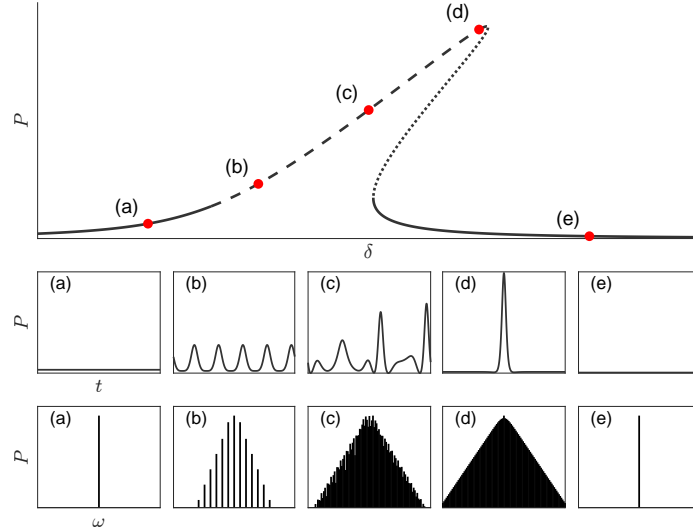


Figure 1.4: Illustration of a detuning sweep following a tilted resonance profile and resulting cavity dynamics underneath. Areas with MI are marked by a dashed line, and the unstable middle branch by a dotted line. Field power profiles at each detuning are shown in the first row and corresponding logarithmic power spectra in the second where the rapid pump field is factored out, making CW solutions constant. Observed dynamics are homogeneous CW solutions (a), (e), Turing pattern (b), chaos (c) and a single temporal cavity soliton (d).

Provided sufficient pump power, a tour of the relevant dynamics can be generated by sweeping the detuning from negative values to positive (figure 1.4). At low detuning, the intracavity field is far from resonance and of low amplitude, matching the pump field in frequency. As the detuning increases towards zero, the field grows in amplitude, and eventually exceeds the MI threshold. Here, the first stable structure (beyond sideband modulation) may be encountered when the intracavity power is large enough to trigger the cascaded FWM process, but weak enough to terminate at a steady-state where the rate of photon production between modes balances out the ones leaving. We then get a subset of excited comb teeth separated by multiples of the cavity FSR, which in the time domain forms a stable periodic pattern or Turing pattern. These structures are not localized since their periodic nature depends on the circular boundary condition

of the resonator, which differentiate them from temporal cavity solitons, encountered later.

If the intracavity power continues to grow, new dynamical regimes start to appear. One possibility is a Hopf bifurcation, resulting in a periodic breathing of previously stationary patterns. At high enough energy the field structure is lost, and the comb enters a chaotic regime known as optical turbulence. This noisy state persists until the bistable region is reached, where it is possible for one or more bright temporal cavity solitons to form, resting on top of a stable CW background corresponding to the lower branch. They circulate inside the cavity and transmit a train of pulses similar to a mode-locked laser, and consequently generate a broad, low-noise frequency comb with phase correlated components separated by one FSR. At high enough detuning, the solitons collapse and return the cavity to a uniform CW state on the lower branch.

1.2.4 Mathematical models

A general starting point to model the dynamics of a Kerr cavity is to directly consider the optical field inside of it. The nature of a traveling wave resonator used in microresonators is to guide the field using total internal reflection so as to eventually return it to its starting point, where it interferes with itself. If we follow the propagating field inside the cavity, we can then identify two repeating stages of its evolution. The field first changes continuously as it travels through the resonator, and then interacts with the pump field when it passes the area of coupling. For simplicity, this area will be approximated as a point, making the interaction act discontinuously on the field as it passes.

We may formalize the above description by partitioning the field evolution into intervals corresponding to its roundtrip time, separated by a periodic boundary condition. This approach yields a so called Ikeda map [19] which can be used to calculate the intracavity field at each roundtrip given knowledge of the last

$$\frac{\partial \psi^m}{\partial \xi} = -\frac{\alpha}{2} \psi^m - is \frac{\partial^2 \psi^m}{\partial \tau^2} + i|\psi^m|^2 \psi^m, \quad (1.3)$$

$$\psi^{m+1}(0, \tau) = \sqrt{1 - \alpha} e^{-i\delta} \psi^m(1, \tau) + \sqrt{\alpha} \psi_{\text{in}}, \quad (1.4)$$

where $\psi^m(\xi, \tau)$ is the normalized slowly varying field envelope at roundtrip m written in terms of the normalized longitudinal coordinate ξ and time τ which describe the field from a frame moving with the group velocity. The model is parameterized by the total cavity loss α , group-velocity dispersion sign s , pump frequency detuning δ and normalized power ψ_{in} . Using the Ikeda map, roundtrip $m + 1$ of the field can be modeled as the continuous propagation inside the resonator (1.3) subject to the time varying boundary condition at $\xi = 0$ from the field in roundtrip m at $\xi = 1$ (corresponding to the cavity length in the normalized coordinate ξ), along with the pump coupling (1.4). The Ikeda map is covered more thoroughly in chapter 2.

A simpler, more widely used model known as the Lugiato-Lefever equation (LLE) [14] can be derived from the Ikeda map [20] which averages the pump boundary condition over one roundtrip

$$\frac{\partial \psi}{\partial \eta} = -(\alpha + i\delta) \psi - is \frac{\partial^2 \psi}{\partial \tau^2} + i|\psi|^2 \psi + \sqrt{\alpha} \psi_{\text{in}}, \quad (1.5)$$

where the slow time η , defined as a continuous extension of the discrete roundtrip number, replaces the longitudinal coordinate ξ as the evolution variable. For the intracavity power regimes usually encountered in microresonators this model is an excellent approximation, accurately predicting most Kerr comb dynamics such as those illustrated in figure 1.4. For large intracavity power it becomes increasingly inaccurate, though, and while it can model bistability it completely ignores the possible overlap of adjacent mode resonances associated with multistability [16]. It is therefore interesting to use both models and compare the results.

In the context of nonlinear optics, the LLE model was first introduced in 1987 to study

transverse pattern formation such as spatial solitons in Kerr cavities through the interplay of two-dimensional diffraction and self-focusing [14]. It was only later adapted to describe temporal or longitudinal patterns using one-dimensional dispersion and self-phase modulation. It is for this reason that one must differentiate between temporal (longitudinal) and spatial (transverse) cavity solitons. For future references, we will only make use of the longitudinal version, unambiguously referred to as the LLE.

Another popular approach not covered in this work is the coupled mode formalism [21], which relates the Fourier amplitudes of each cavity mode in a coupled system of differential equations. The model therefore resides entirely in the frequency domain, unlike the Ikeda map and LLE which are time domain descriptions.

1.3 Problem

The main problem addressed in this thesis work is the relationship between parameters of a pumped optical Kerr cavity and the resulting dynamics on a theoretical level. By exploring models of such nonlinear cavities with regard to frequency comb formation, insight is generated which could guide development of real world systems or experimental searches of predicted phenomena.

1.3.1 Goals

Specifically, a mapping is to be produced from parameter areas to different dynamical regimes relevant to frequency comb generation including Turing patterns, chaos, solitons and homogeneous CW solutions. Both the Ikeda map and Lugiato-Lefever equation are used to this end, translating parameters to dynamics. The Ikeda map in particular will also be examined in the high-power regime in search of the super energetic solitons described in [16], in order to determine parameter regions commensurate with their existence.

1.3.2 Methods

The methods used to explore each model can be divided into analytical and numerical categories. In the analytical approach, the parameter space is narrowed down by determining what regions contain modulational instability with respect to the LLE, which is one known path for the intracavity field to transition out of a homogeneous CW solution and potentially self-organize to a stable pattern [10]. Further, the exact CW solutions with respect to both the LLE and Ikeda map are found, which reveal both the expected behavior in regions lacking MI and regions with bi- and multistability. Numerical methods are then finally used to attain solutions from the models in parameter areas of interest. An integration scheme known as the split-step Fourier method is employed both for the Ikeda map and LLE.

1.3.3 Delimitations

The modeling of Kerr cavity dynamics will only include second order dispersion and linear attenuation. Further, while both normal and anomalous dispersion is covered theoretically, only the latter is considered in numerical simulations. The models used to describe the intracavity field will be limited to the Ikeda map and LLE, with the modal expansion approach not treated. In the analytical treatment of the models, only the LLE will be subject to a stability analysis, and the more nuanced stability regions of the Ikeda map will be ignored. The classification of dynamical regimes will mainly focus on stationary patterns with respect to individual roundtrips and exclude periodic behavior such as breathers and period doubling (though examples of breathers will be encountered). Finally, the search for super cavity solitons will be constrained to the first excited state [16] beyond the solitons modeled by the LLE.

1.4 Thesis structure

The first part of the document comprising chapter 2 through 5 reviews the theoretical foundations and tools used in the work, with no fundamentally new results. In particular, chapter 2 outlines an Ikeda map derivation through the combination of nonlinear waveguide propagation starting from Maxwell's equations [13][22] and pump field coupling [23]. On the way, relevant physics are discussed along with justifications for their inclusion or exclusion. The full Ikeda map model is then finally stripped of as many parameters as possible by rescaling the variables and applying mild assumptions about the system (critical coupling). Chapter 3 presents a derivation of the (normalized) Lugiato-Lefever equation from the Ikeda map described in the previous chapter similar to [24]. In chapter 4 analytical methods are presented. The Lugiato-Lefever equation is examined for the conditions required for modulational instability [24] and exact CW solutions are calculated for both the LLE and Ikeda map [16]. Chapter 5 covers numerical methods, where the general theory behind operator splitting [25] is first discussed and then applied on both the Ikeda map and LLE to produce the split-step Fourier integration scheme [13].

The second part of the document contains results partially or fully original to the current work. Chapter 6 describes the design process behind the numerical software developed, together with an overview of its functionality and the workflow used to conduct simulations. Chapter 7 documents the results produced through simulations with comments. Here, the parameter space supporting super cavity solitons [16] in the high-energy regions of the Ikeda map constitutes a new result, and the low-power regions explored for both the LLE and Ikeda map display an intricate boundary delimiting stationary patterns not previously reported in theoretical examinations to the author's knowledge. Finally, chapter 8 provides conclusions, reflections and areas of future work.

Chapter 2

The Ikeda map

In this chapter the central model describing the dynamics of a nonlinear optical cavity, the so called Ikeda map [19], is described. With this model we are granted a rich description of the evolving fields inside the cavity that will serve as a basis for further investigation, both through approximations and numerical methods.

In section 2.1 we acquire the propagation equation of an optical field in a cavity subject to a Kerr nonlinearity, starting from Maxwell's equations. Several assumptions will be employed in its derivation, most notably that of a quasi-monochromatic intracavity field centered on the external pump frequency. The result will be a damped, nonlinear Schrödinger equation, modeling group velocity dispersion, self-phase modulation and attenuation of the field envelope as it propagates through the resonator. Section 2.2 is dedicated to the boundary condition which connects the fields from successive roundtrips, in addition to the pump interaction [23]. It will also account for frequency detuning of the pump field away from cavity resonance, causing a phase mismatch between it and the returning field. The final section 2.3 will be aimed at reducing the number of model parameters, both through variable scaling and appropriate assumptions.

2.1 Pulse propagation

In this section we develop an equation describing the continuous evolution of an optical pulse in the interim of boundary effects between successive roundtrips through the resonator. The point of departure is Maxwell's equations in matter

$$\nabla \cdot \mathbf{D} = \rho, \quad (2.1)$$

$$\nabla \cdot \mathbf{B} = 0, \quad (2.2)$$

$$\nabla \times \mathbf{E} = -\frac{\partial \mathbf{B}}{\partial t}, \quad (2.3)$$

$$\nabla \times \mathbf{H} = \frac{\partial \mathbf{D}}{\partial t} + \mathbf{J}, \quad (2.4)$$

which relate the electric and magnetic field strengths \mathbf{E} , \mathbf{H} , electric and magnetic flux densities \mathbf{D} , \mathbf{B} , with the free charge density ρ and free current density \mathbf{J} . Further, the material influence on the fields is accounted for through the magnetization density \mathbf{M} and polarization density \mathbf{P} in the constitutive relations

$$\mathbf{D} = \epsilon_0 \mathbf{E} + \mathbf{P}, \quad (2.5)$$

$$\mathbf{B} = \mu_0 (\mathbf{H} + \mathbf{M}), \quad (2.6)$$

where ϵ_0 and μ_0 , the permittivity and permeability of free space, relate flux densities and field strengths in absence of material effects.

Together with the boundary conditions for the problem, this set of equations constitutes a complete description of the fields inside the resonator provided we know \mathbf{P} and \mathbf{M} . In general, the magnetic properties of materials at optical frequencies are very low, so we set $\mathbf{M} = 0$. Further, we set the free charge density $\rho = 0$ and free current density $\mathbf{J} = 0$ as the materials of interest are dielectric. This leaves the polarization density \mathbf{P} induced by the field strength \mathbf{E} as the quantity of interest describing the influence of the material.

Since we seek a wave description of the optical field, we proceed in the usual fashion by taking the curl of (2.3)

$$\nabla \times \nabla \times \mathbf{E} = \nabla \times \left(-\frac{\partial \mathbf{B}}{\partial t} \right). \quad (2.7)$$

The left hand side is expanded using the vector calculus identity $\nabla \times \nabla \times \mathbf{E} = \nabla (\nabla \cdot \mathbf{E}) - \nabla^2 \mathbf{E}$ and we may eliminate the first term by assuming $\nabla \cdot \mathbf{E} = 0$, which is true in a homogeneous medium far from the boundary, neglecting nonlinearity [9]. Rewriting the right hand side using (2.6), (2.4) and (2.5) then yields the wave equation¹

$$\nabla^2 \mathbf{E} - \frac{1}{c^2} \frac{\partial^2 \mathbf{E}}{\partial t^2} = \mu_0 \frac{\partial^2 \mathbf{P}}{\partial t^2}, \quad (2.8)$$

where $c = 1/\sqrt{\epsilon_0 \mu_0}$ is the speed of light in vacuum. We interpret the right hand side of (2.8) as a forcing term, in lieu of which solutions reduce to simple plane waves in vacuum (barring confinement effects of the cavity). In this sense, the polarization \mathbf{P} and its relationship to the electric field \mathbf{E} will dictate all noteworthy characteristics of wave propagation inside the cavity, giving rise to phenomena such as group-velocity dispersion and self-phase modulation (both of which are important in the formation of frequency combs).

To proceed further we need the exact relation between \mathbf{P} and \mathbf{E} , and to this end we start by decomposing the polarization in a linear and nonlinear component with respect to the electric field strength

$$\mathbf{P}(\mathbf{r}, t) = \mathbf{P}_L(\mathbf{r}, t) + \mathbf{P}_{NL}(\mathbf{r}, t). \quad (2.9)$$

We next note that the nonlinear polarization \mathbf{P}_{NL} in general is small compared to the linear one, which suggests the approach of treating the linear case $\mathbf{P}_{NL} = 0$ first and adding the nonlinear effects as a perturbation. We will return to address the nonlinear contribution in a later section along with a brief discussion on its physical origins, where we will see that it takes the form of a small intensity dependent adjustment to the refractive index – the Kerr effect. Proceeding with the linear wave equation, we have

$$\nabla^2 \mathbf{E} - \frac{1}{c^2} \frac{\partial^2 \mathbf{E}}{\partial t^2} = \mu_0 \frac{\partial^2 \mathbf{P}_L}{\partial t^2}. \quad (2.10)$$

While indeed linear, the induced polarization \mathbf{P}_L in a dispersive medium is not an instantaneous function of the applied electric field \mathbf{E} at a certain point in time but rather of its frequency content, with the strength of the response roughly correlated with the proximity of the field frequency to electronic resonances in the dielectric medium [13]. Defining the frequency domain quantities through the Fourier transform²

$$\hat{\mathbf{E}}(\mathbf{r}, \omega) = \int_{-\infty}^{\infty} \mathbf{E}(\mathbf{r}, t) \exp(i\omega t) dt, \quad (2.11)$$

$$\hat{\mathbf{P}}(\mathbf{r}, \omega) = \int_{-\infty}^{\infty} \mathbf{P}(\mathbf{r}, t) \exp(i\omega t) dt, \quad (2.12)$$

¹The wave equation for the accompanying magnetic field strength \mathbf{H} can be acquired analogously.

²Various Fourier transforms are used in the literature.

we may express this relationship succinctly in the frequency domain as

$$\hat{\mathbf{P}}_L(\mathbf{r}, \omega) = \epsilon_0 \hat{\chi}^{(1)}(\omega) \hat{\mathbf{E}}(\mathbf{r}, \omega), \quad (2.13)$$

where $\hat{\chi}^{(1)}(\omega)$ is the frequency dependent first order susceptibility. In general, $\hat{\chi}^{(1)}(\omega)$ is a complex quantity, such that a sinusoidal electric field of frequency ω_0 would excite a polarization of the same frequency but scaled $\epsilon_0 |\hat{\chi}^{(1)}(\omega_0)|$ and phase shifted $\arg \hat{\chi}^{(1)}(\omega_0)$. The phase difference between the polarization and the electric field incurred by a nonzero imaginary part of the susceptibility creates attenuation in the material, so called dielectric loss. To simplify our analysis, we discard the imaginary part for now and return to add losses later in the same vein as nonlinearity. Additionally, in its full generality, $\hat{\chi}^{(1)}(\omega)$ takes the form of a tensor in order to model birefringent media. We will however assume that the electric field is polarized, so a scalar relation will suffice.

The form of (2.13) motivates a migration of the wave equation (2.10) to the frequency domain, which, using the same Fourier transform as before, yield the Helmholtz equation

$$\nabla^2 \hat{\mathbf{E}} + \frac{\omega^2}{c^2} n^2(\omega) \hat{\mathbf{E}} = 0, \quad (2.14)$$

where $n^2(\omega) = 1 + \hat{\chi}^{(1)}(\omega)$ defines the (frequency dependent) refractive index, and where we used (2.13). The frequency domain representation of the electric field $\hat{\mathbf{E}}(\mathbf{r}, \omega)$ is now a complex vector, carrying both magnitude and phase information at each frequency and location.

Constraining the search for solutions to transverse electric fields, there are two possible polarizations along each axis perpendicular to the propagation direction, denoted \hat{x} and \hat{y} . Assuming $\hat{\mathbf{E}} = \hat{y}\hat{E}$ in (2.14) reduces it to a scalar equation

$$\nabla^2 \hat{E} + \frac{\omega^2}{c^2} n^2(\omega) \hat{E} = 0. \quad (2.15)$$

To proceed further in solving (2.15) requires knowledge of the resonator geometry, but we expect that the electric field travels in a propagation mode, that is, with a constant transverse field profile $F(x, y)$ modulated in the direction of propagation z

$$\hat{E}(\mathbf{r}, \omega) = F(x, y) \exp[i\beta(\omega)z], \quad (2.16)$$

where $\beta(\omega)$ is the propagation constant³. Substituting (2.16) in (2.15), we get

$$\nabla_T^2 F + \left(\frac{\omega^2}{c^2} n^2 - \beta^2 \right) F = 0, \quad (2.17)$$

where

$$\nabla_T^2 = \frac{\partial^2}{\partial x^2} + \frac{\partial^2}{\partial y^2}. \quad (2.18)$$

Similar to a single-mode fiber, we assume that there exists exactly one solution β , F to the eigenvalue problem (2.17) for each ω in the frequency range we are interested in, where β is real. To represent a guided mode we further expect each such β , by inspection of (2.17), to produce the qualitative behavior of $\nabla_T^2 F \propto -F$ (oscillatory) inside the resonator and $\nabla_T^2 F \propto F$ (decaying) outside.

To solve (2.17) for F and β , one would either adopt a suitable coordinate system and further separate the variables, or, more generally, employ mode solver software. This would grant a complete description of the evolution of all imaginable wave profiles in the resonator, but we are

³related to the wavenumber through the effective refractive index, accounting for the relatively small dispersive effects of the mode geometry as well as the material dispersion.

interested in the specific case of a quasi-monochromatic field, that is, a field whose frequency content is only appreciable in a relatively small interval. To make use of this simplifying assumption we first note that the z -dependence of \hat{E} in (2.16) can be restated as the differential equation

$$\frac{\partial \hat{E}}{\partial z} = i\beta(\omega)\hat{E}, \quad (2.19)$$

where we assume a propagation in the positive longitudinal direction z . We then expand $\beta(\omega)$ in a Taylor series around the center ω_0 of the small frequency interval, which is justified as we are only concerned with faithfully recreating the evolution of frequencies in this neighborhood,

$$\frac{\partial \hat{E}}{\partial z} \approx i \left[\beta_0 + \beta_1(\omega - \omega_0) + \frac{1}{2}\beta_2(\omega - \omega_0)^2 \right] \hat{E}, \quad (2.20)$$

where

$$\beta_i = \left. \frac{d^i \beta}{d\omega^i} \right|_{\omega=\omega_0}. \quad (2.21)$$

This is equivalent to the slowly varying envelope approximation in the time domain, where the second derivative with respect to z of the wave equation governing the pulse envelope is neglected [13]. The Taylor series coefficients β_i can be identified with characteristic properties of wave propagation. The first coefficient β_0 is the spatial frequency of the rapidly varying carrier wave on top of which the pulse is modulated, β_1 is the inverse group velocity which is the propagation speed of the pulse envelope, and β_2 the group velocity dispersion, expressing the widening of the pulse envelope over time. This is a much more economical representation compared to the full $\beta(\omega)$ which generally do not admit a closed form solution, and higher orders of dispersion can easily be included in (2.20) if desired.

The expansion (2.20) also offers a convenient juncture to account for perturbations in the refractive index [22]. Using first order perturbation theory on (2.17), the perturbed index $n' = n + \delta n$, transverse field $F' = F + \delta F$ and propagation constant $\beta' = \beta + \delta\beta$ is inserted and terms common to the unperturbed solution are removed, yielding an equation for the perturbations. If this equation is then multiplied by the complex conjugate F^* and integrated over the transverse mode area, we get

$$\delta\beta = \frac{\omega_0}{c} \frac{\iint \delta n |F|^2 dx dy}{\iint |F|^2 dx dy}, \quad (2.22)$$

where the frequency was approximated as fixed on ω_0 . Up to first order in the perturbation δn , the field profile remains unchanged, that is, $\delta F = 0$. We will return at a later point to evaluate (2.22) further given specific perturbations to the index, and will for now just include it in the expansion (2.20), giving

$$\frac{\partial \hat{E}}{\partial z} = i \left[\beta_0 + \beta_1(\omega - \omega_0) + \frac{1}{2}\beta_2(\omega - \omega_0)^2 + \delta\beta \right] \hat{E}. \quad (2.23)$$

Equation (2.23) would make a sufficient model of propagation if transformed back to the time domain, but would describe the field in its entirety when the essential feature for our purposes is the pulse envelope. If we factor out the rapid carrier wave from a time domain representation of the field, we can identify this slowly varying envelope $A(z, t)$,

$$E(\mathbf{r}, t) = \frac{1}{2} \left(F(x, y) A(z, t) \exp[i(\beta_0 z - \omega_0 t)] + \text{c.c.} \right), \quad (2.24)$$

where c.c. is the complex conjugate of the previous term. It is convenient to represent the time

domain field by just the first term

$$E(\mathbf{r}, t) = \frac{1}{2} F(x, y) A(z, t) \exp[i(\beta_0 z - \omega_0 t)], \quad (2.25)$$

and keep in mind that the real field is recovered through (2.24), with linearity ensuring this complex representation is equivalent to the physical field. To produce the governing equation of $A(z, t)$ we Fourier transform (2.25)

$$\hat{E}(\mathbf{r}, \omega) = \frac{1}{2} F(x, y) \hat{A}(z, \omega - \omega_0) \exp(i\beta_0 z), \quad (2.26)$$

and insert the result in (2.23). Simplifying, we get

$$\frac{\partial}{\partial z} \hat{A}(z, \omega - \omega_0) = i \left[\beta_1(\omega - \omega_0) + \frac{1}{2} \beta_2(\omega - \omega_0)^2 + \delta\beta \right] \hat{A}(z, \omega - \omega_0). \quad (2.27)$$

Finally, (2.27) is inverse Fourier transformed through

$$A(t) = \frac{1}{2\pi} \int_{-\infty}^{\infty} \hat{A}(\omega) e^{-i\omega t} d\omega, \quad (2.28)$$

to yield

$$\frac{\partial A}{\partial z} = -\beta_1 \frac{\partial A}{\partial t} - i \frac{\beta_2}{2} \frac{\partial^2 A}{\partial t^2} + i\delta\beta A, \quad (2.29)$$

where the integral in (2.28) is evaluated through a change of variables. Equation (2.29) describes the space and time evolution of the envelope $A(z, t)$ of an optical pulse. As it propagates with the group velocity $v_g = 1/\beta_1$, it is subject to group velocity dispersion β_2 which generally serves to broaden the pulse over time due to the different propagation speeds of each frequency component. This is evident from the fact that $\beta_2 = 0$ would imply, up to second order dispersion, a proportional relationship between the propagation constant and frequency around ω_0 , which translates to uniform propagation speed of each frequency component in that neighborhood. Another consequence of a non-zero β_2 is the so called chirping of pulses where higher frequency components bunch up in the front or back of the pulse, depending on the sign of β_2 , creating a local frequency variation along it. While important in many scenarios of pulse propagation [13], chirping will play a minor role for our purposes and will not be covered further.

2.1.1 Attenuation

We now seek to include a reasonably simple description of attenuation in our pulse propagation equation. One straightforward way to model intrinsic loss is to allow the refractive index to take on a complex value, where the imaginary part then describes the material absorption due to dielectric loss. This implies exponential decay of the field as it propagates through the material, dissipating the field energy as heat.

Several other mechanisms of attenuation are in general also significant depending on the frequency, for example the ubiquitous phenomena of Rayleigh scattering caused by small fluctuations in the material composition [13]. We will however constrain our analysis to dielectric loss, with the justification that other linear processes act similarly. We will also assume that the loss spectrum is constant, as we only model a narrow set of frequencies over which dispersion is expected to vary much quicker. We will finally assume that the loss is low, owing to the high Q cavities employed in microresonators.

A complex refractive index translates to a complex permittivity, and therefore a complex susceptibility. Treating the refractive index as complex is then formally equivalent to accounting for the previously discarded imaginary part of the susceptibility. We define the complex refractive

index [13] as

$$n' = n_0 + i \frac{\alpha_i c}{2\omega_0}, \quad (2.30)$$

where n_0 is the previous real refractive index evaluated at ω_0 , and α_i the absorption coefficient. We then interpret the imaginary part as a small perturbation

$$\delta n = i \frac{\alpha_i c}{2\omega_0}, \quad (2.31)$$

which in (2.22) gives us

$$\delta \beta = i \frac{\alpha_i}{2}, \quad (2.32)$$

which inserted in (2.29) finally result in the propagation equation

$$\frac{\partial A}{\partial z} = -\frac{\alpha_i}{2} A - \beta_1 \frac{\partial A}{\partial t} - i \frac{\beta_2}{2} \frac{\partial^2 A}{\partial t^2}. \quad (2.33)$$

The pulse amplitude now experiences damping as it propagates through the resonator. The factor $1/2$ implies that $|A|^2$ decay at a rate α_i , which can be verified by differentiating with respect to z and using (2.33).

There are generally more mechanisms of attenuation that cannot be accounted for through the linear term in (2.33). One such case is two-photon absorption, which becomes relevant when individual photon energies exceed half the band gap of semiconductor materials. It then manifests as an intensity dependent absorption term [13], analogously to the nonlinear refractive index, covered in the next section. Another very relevant phenomenon in resonators is coupling loss, which is the energy transmitted as output. A measure of the total capacity to retain energy is the so called total cavity loss, defined as the combined intrinsic and coupling loss $\alpha = (\alpha_i L + \theta)/2$, where L is the resonator circumference and θ is the power coupling factor of the cavity [26].

2.1.2 Nonlinearity

We now consider the effects of a nonlinear polarization P_{NL} induced by the electric field on the propagation equation (2.29). Maintaining the assumption of a polarized field $\hat{\mathbf{E}} = \hat{y}\hat{E}$, we may expand the time domain polarization as

$$P(\mathbf{r}, t) = \epsilon_0 \left(\chi^{(1)} E(\mathbf{r}, t) + \chi^{(2)} E^2(\mathbf{r}, t) + \chi^{(3)} E^3(\mathbf{r}, t) + \dots \right), \quad (2.34)$$

where we now consider it an instantaneous function of the electric field with respect to time. The nonlinear polarization is then identified as the terms of order above unity. While generally small, these nonlinear terms open channels of interaction between frequency components, and the superposition principle is hence no longer applicable.

These wave mixing processes are understood from a classical perspective as the distributed radiating effect of the nonlinear polarization, while the quantum mechanical view is instead that of simultaneous creation and annihilation of several photons at once, subject to energy and momentum conservation. The resulting frequencies/photons will however only be of consequence if they are produced as to constructively interfere, which generally requires the optical system to be designed according to a phase matching condition.

The number of frequency components or photons which participate in a mixing process is determined by the order of the nonlinearity at play, and we therefore examine each term in (2.34) to determine its relevance for our purposes. In brief, the induced polarization in a dielectric stems from the movement of charges under an applied field, e.g. rotation of dipoles, displacement of electrons, etc. The degree of movement can qualitatively be likened to the elongation of a spring, in which case the first order susceptibility $\chi^{(1)}$ represents a proportional restoring force.

The second order susceptibility $\chi^{(2)}$ is the first correction for asymmetry, that is, a restoring force dependent on direction, and gives rise to three-wave mixing phenomena like second-harmonic generation. This $\chi^{(2)}$ term is non-zero only if the material lacks inversion symmetry, i.e. is not unchanged by the transformation $\mathbf{r} \rightarrow -\mathbf{r}$. However, inversion symmetry holds for most materials of interest, e.g. SiO_2 , and consequently we set $\chi^{(2)} = 0$.

This leaves the third order susceptibility $\chi^{(3)}$ as the primary contributor of nonlinear effects to the polarization which, in the spring analogy, equates to a non proportional restoring force⁴. A relatively large number of interactions between different frequency components are available through a third order nonlinearity, collectively referred to as four wave-mixing [9]. To be exact,

$$P^{(3)}(\mathbf{r}, t) = \epsilon_0 \chi^{(3)} \left(E_1(\mathbf{r})e^{i\omega_1 t} + E_2(\mathbf{r})e^{i\omega_2 t} + E_3(\mathbf{r})e^{i\omega_3 t} + \text{c.c.} \right)^3 \quad (2.35)$$

contains 44 frequency components, but since most of these interfere destructively without phase matching, they will not be studied further. One exception to the previous statement can be observed through

$$P^{(3)}(\mathbf{r}, t) = \epsilon_0 \chi^{(3)} (E(\mathbf{r}) \cos \omega t)^3 = \frac{1}{4} \epsilon_0 \chi^{(3)} E^3(\mathbf{r}) \cos 3\omega t + \frac{3}{4} \epsilon_0 \chi^{(3)} E^3(\mathbf{r}) \cos \omega t. \quad (2.36)$$

The second term in the right hand side of (2.36) is automatically in phase with the electric field at all points and so does not need explicit phase matching to contribute. Ignoring the first term which does require phase matching, we may write

$$P^{(3)}(\mathbf{r}, t) = \epsilon_0 \epsilon_{NL} E(\mathbf{r}, t), \quad (2.37)$$

where

$$\epsilon_{NL} = \frac{3}{4} \chi^{(3)} |E(\mathbf{r}, t)|^2 \quad (2.38)$$

is the nonlinear relative permittivity. Since $n = \epsilon^{1/2}$, this implies a small adjustment to the refractive index

$$n' = \left(1 + \chi^{(1)} + \epsilon_{NL} \right)^{1/2} \approx n_0 + \frac{\epsilon_{NL}}{2n_0}, \quad (2.39)$$

where we have used $n_0 = (1 + \chi^{(1)})^{1/2}$ for the unperturbed index evaluated at ω_0 and that ϵ_{NL} is small. This can be presented in a more standard form revealing an intensity dependent refractive index, the so called Kerr effect

$$n' = n_0 + n_2 I, \quad (2.40)$$

where $I = n_0 \epsilon_0 c |E|^2 / 2$ is the intensity measured in W/m^2 and $n_2 = 3\chi^{(3)} / 4n_0^2 \epsilon_0 c$ the nonlinear coefficient of the material measured in m^2/W . We interpret the second term in (2.40) as a perturbation to the refractive index

$$\delta n = n_2 I = \frac{1}{8} n_2 n_0 \epsilon_0 c |F|^2 |A|^2, \quad (2.41)$$

where we used $|E|^2 = |F|^2 |A|^2 / 4$ from (2.25), which is again evaluated through (2.22) to get the perturbation of the propagation constant

$$\delta \beta = \kappa |A|^2, \quad (2.42)$$

where

$$\kappa = \frac{\omega_0 n_2 n_0 \epsilon_0}{8} \frac{\iint |F|^4 dx dy}{\iint |F|^2 dx dy}. \quad (2.43)$$

⁴Equivalent to a forced Duffing oscillator without damping [27].

Inserting (2.42) in (2.29) we finally get

$$\frac{\partial A}{\partial z} = -\beta_1 \frac{\partial A}{\partial t} - i \frac{\beta_2}{2} \frac{\partial^2 A}{\partial t^2} + i\kappa |A|^2 A. \quad (2.44)$$

We recognize (2.44) as a nonlinear Schrödinger equation where the evolution along z now acquires a nonlinear phase contribution (self-phase modulation). The perturbation used in deriving (2.44) is dependent on A , which is not constant in time like assumed in the perturbation analysis. We justify this transgression by noting that the propagation constant β can be viewed simultaneously as a function of frequency and time if we retrieve the frequency dependence from the rapid pump field at ω_0 , and the comparatively slow time dependence from A [22].

2.1.3 Propagation equation

Combining the effects of attenuation from (2.33) and nonlinear phase modulation from (2.44), we arrive at a damped, nonlinear Schrödinger equation for the pulse envelope,

$$\frac{\partial A}{\partial z} = -\frac{\alpha_i}{2} A - \beta_1 \frac{\partial A}{\partial t} - i \frac{\beta_2}{2} \frac{\partial^2 A}{\partial t^2} + i\kappa |A|^2 A. \quad (2.45)$$

The envelope $A(z, t)$ is mathematically well defined, but lacks an interpretation in terms of physical units. We note that the power flow P through a cross section of the resonator is

$$P = \iint I \, dx dy = \left(\frac{n_0 \epsilon_0 c}{8} \iint |F|^2 \, dx dy \right) |A|^2, \quad (2.46)$$

where we again used the intensity $I = n_0 \epsilon_0 c |E|^2 / 2$ and $|E|^2 = |F|^2 |A|^2 / 4$ from (2.25). If we introduce the normalized envelope

$$A'(z, t) = \frac{1}{2} \sqrt{\frac{n_0 \epsilon_0 c \iint |F|^2 \, dx dy}{2}} A(z, t), \quad (2.47)$$

then (2.46) gives $P = |A'|^2$, that is, the amplitude A' is measured in units such that $|A'|^2$ marks the total power flowing through the resonator at a point. Reformulating the pulse propagation equation (2.45) in terms of A' and dropping the primed notation for convenience, we get

$$\frac{\partial A}{\partial z} = -\frac{\alpha_i}{2} A - \beta_1 \frac{\partial A}{\partial t} - i \frac{\beta_2}{2} \frac{\partial^2 A}{\partial t^2} + i\gamma |A|^2 A, \quad (2.48)$$

where

$$\gamma = \frac{\omega_0 n_2}{c A_{\text{eff}}} \quad (2.49)$$

is the nonlinear coefficient and where

$$A_{\text{eff}} = \frac{\left(\iint |F|^2 \, dx dy \right)^2}{\iint |F|^4 \, dx dy} \quad (2.50)$$

is the effective mode area. The effective mode area is the only mention of the transverse field distribution F in the final model, and we see that smaller mode areas result in a stronger nonlinearity due to the field being more concentrated. For similar derivations of the pulse propagation equation, see [22][13].

A brief discussion on the interpretation of (2.48) is warranted. For context, partial differential equations describing time-space evolution of physical phenomena, e.g. the heat equation, can sometimes lend themselves to a simple interpretation where the spatial dependence of a solution

constitutes the system "state" which is advanced by moving in the time direction. This interpretation also mirrors the most obvious method of generating numerical solutions to such problems, given initial spatial data.

One might try to apply this perspective to our case by imagining successive snapshots of the spatial field distribution inside the resonator, each one generating the next. It is quickly realized, however, that equation (2.48) is better suited for expressing the spatial evolution of the field, rather than the temporal.

A second attempt instead makes us think of the temporal axis as the "state" to be advanced in the spatial direction. Each point in the resonator then has attached a time window containing the field amplitude as measured when passing through it. Using (2.48) we can subsequently generate the next time view of the field that would be measured from a point incrementally farther along the resonator. We choose the duration of this window to be the time required for the field to complete one roundtrip traveling at the group velocity $v_g = 1/\beta_1$, which is the longest interval the pulse propagation equation remains valid before encountering the boundary condition, to be derived in the next section.

We can enjoy one more simplification of (2.48) by noting that the drift of the pulse with respect to the group velocity is uninteresting if we only wish to study the evolution of its profile. To this end we introduce new variables in (2.48) such that each spatial point is associated with a time scale which is shifted by the time it takes the group velocity $v_g = 1/\beta_1$ to reach it, thereby nullifying the group velocity drift,

$$t' = t - \beta_1 z, \quad (2.51)$$

$$z' = z, \quad (2.52)$$

giving us

$$\frac{\partial A}{\partial z} = -\frac{\alpha_i}{2} A - i\frac{\beta_2}{2} \frac{\partial^2 A}{\partial t^2} + i\gamma |A|^2 A, \quad (2.53)$$

where we again have dropped the primed notation. The variable t now represents the retarded time with respect to the group velocity, and effectively allow us to observe the pulse from a frame moving alongside it. From this perspective the group velocity term vanishes and the pulse appears stationary (figure 2.1).

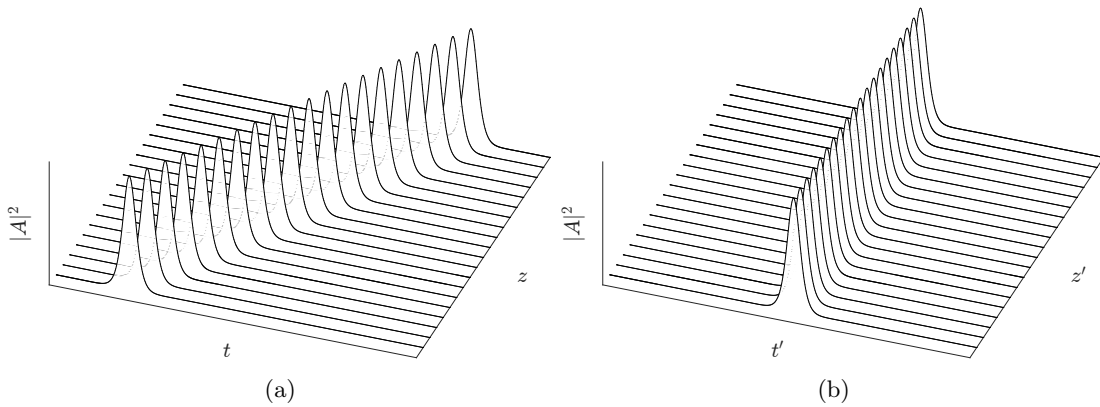


Figure 2.1: A pulse propagating through the resonator viewed from a laboratory frame (a) and a moving frame (b).

2.2 Boundary condition

On its journey through the resonator, the field envelope A evolves continuously as prescribed by the equation (2.53) derived in the previous section. When it reaches the point of coupling to the external pump field, however, some of the pump field is passed into the resonator, while a part of the intracavity field is transmitted out. In this section, we derive the boundary condition which, in our model, acts to discontinuously impart these effects on the field as it passes over the point of coupling.

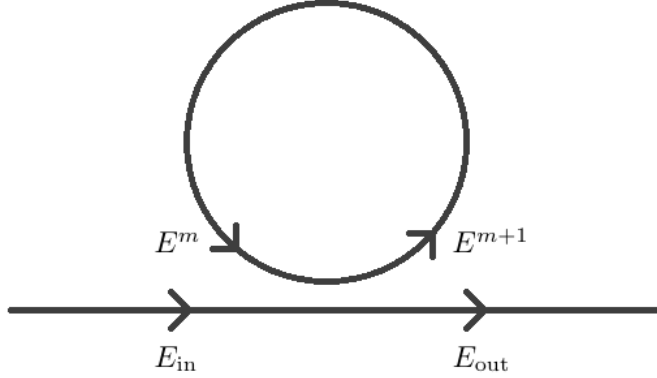


Figure 2.2: Resonator coupling.

A typical scenario for pumping an optical cavity is by routing a waveguide containing a CW laser field near the cavity such that their evanescent fields overlap (figure 2.2) [18]. The strength of the resulting coupling is modeled by the dimensionless intensity coupling coefficient θ , describing the fraction of power transferred from the waveguide to the resonator (and vice versa). Imagining for simplicity that the coupling happens at a single point and is lossless, the complex electric fields crossing can be described by a unitary scattering matrix [23]

$$\begin{bmatrix} E^{m+1}(0, t) \\ E_{\text{out}}(t) \end{bmatrix} = \begin{bmatrix} \sqrt{1-\theta} & i\sqrt{\theta} \\ i\sqrt{\theta} & \sqrt{1-\theta} \end{bmatrix} \begin{bmatrix} E^m(L, t) \\ E_{\text{in}}(t) \end{bmatrix}, \quad (2.54)$$

where we assume that the fields are polarized scalar quantities with a one-dimensional spatial dependence expressed in the transformed coordinates defined in (2.51), (2.52). Further, L is the distance of one roundtrip, and the superscripts of the intracavity field indicate what roundtrip the field belongs to. Only the equation corresponding to the top row of the matrix is relevant for the evolution of the intracavity field,

$$E^{m+1}(0, t) = \sqrt{1-\theta}E^m(L, t) + i\sqrt{\theta}E_{\text{in}}(t), \quad (2.55)$$

and to be compatible with (2.53) we need to express the fields in terms of their normalized slowly varying envelopes. Factoring all the fields in (2.55) into their envelope and carrier wave, evaluated at $z = L$ for roundtrip m and $z = 0$ for roundtrip $m + 1$, yields

$$A^{m+1}(0, t)e^{i(\beta_0 0 - \omega_0 t)} = \sqrt{1-\theta}A^m(L, t)e^{i(\beta_0 L - \omega_0 t)} + \sqrt{\theta}A_{\text{in}}e^{i(\beta_0 0 - \omega_0 t)}, \quad (2.56)$$

where we have also taken the liberty of changing the arbitrary phase of the input field to eliminate the imaginary unit. This immediately simplifies to

$$A^{m+1}(0, t) = \sqrt{1-\theta}e^{i\beta_0 L}A^m(L, t) + \sqrt{\theta}A_{\text{in}}. \quad (2.57)$$

In this representation, the pump field appears as a constant A_{in} since it is by definition a scaled version of the carrier wave. It is also seen that the field from the previous roundtrip has acquired a phase difference relative to the carrier wave at the coupling point $z = L$ due to having propagated one roundtrip. If this phase is an integer multiple of 2π , the resonance condition is met, and the circulating field interferes constructively with the pump field. If this condition is not met, however, the pump laser is said to be detuned, and the field from the previous roundtrip gets a phase contribution δ between $-\pi$ and $+\pi$ depending on the closest resonance, which is calculated as $\beta_0 L = 2\pi l - \delta$ where l is the number of the resonance [16], essentially implementing a modulo operation.

We then obtain the time varying boundary condition

$$A^{m+1}(0, t) = \sqrt{1 - \theta} e^{-i\delta} A^m(L, t) + \sqrt{\theta} A_{\text{in}}, \quad (2.58)$$

which together with the pulse propagation equation (2.53) complete the Ikeda map. Through (2.58), the field envelope $A^{m+1}(0, t)$ at the beginning of a roundtrip is expressed in terms of the field from the previous roundtrip $A^m(L, t)$ and the pump field A_{in} .

2.2.1 Critical coupling

In the previous section, only the equation corresponding to the top row of (2.54) was studied so as to understand the intracavity dynamics. It is however also instructive to consider the output E_{out} from the system in its entirety for a given input E_{in} under certain simplifying conditions. Assuming zero detuning and a negligible phase shift from the nonlinearity, we have a resonant CW intracavity field which is only affected by the intrinsic absorption α_i over one roundtrip. This allows us to write $E^m(L, t) = \exp(-\alpha_i L/2) E^m(0, t)$ which inserted in the scattering matrix relation (2.54) gives a top row equation which can be solved for the intracavity field

$$E(t) = \frac{i\sqrt{\theta}}{1 - \exp(-\alpha_i L/2)\sqrt{1 - \theta}} E_{\text{in}}(t), \quad (2.59)$$

where we assume $E^{m+1}(0, t) = E^m(0, t) = E(t)$, since we expect a stationary, resonant CW field in the absence of nonlinearity. The bottom row equation describing the system output E_{out} becomes

$$E_{\text{out}}(t) = i\sqrt{\theta} \exp(-\alpha_i L/2) E(t) + \sqrt{1 - \theta} E_{\text{in}}(t), \quad (2.60)$$

which with (2.59) after simplification yields

$$E_{\text{out}}(t) = \frac{\sqrt{1 - \theta} - \exp(-\alpha_i L/2)}{1 - \exp(-\alpha_i L/2)\sqrt{1 - \theta}} E_{\text{in}}(t). \quad (2.61)$$

This is the desired input-output relation for the electric fields. A more physically useful relation is found by taking the squared complex modulus

$$|E_{\text{out}}(t)|^2 = \left| \frac{\sqrt{1 - \theta} - \exp(-\alpha_i L/2)}{1 - \exp(-\alpha_i L/2)\sqrt{1 - \theta}} \right|^2 |E_{\text{in}}(t)|^2, \quad (2.62)$$

which relates the input and output power of the system in resonance. The crucial feature to note for our purposes is that choosing the power coupling factor θ so that

$$\sqrt{1 - \theta} = \exp(-\alpha_i L/2) \quad (2.63)$$

results in zero output power. In the limit of low intrinsic roundtrip loss and power coupling, jointly constituting a low total cavity loss $\alpha = (\alpha_i L + \theta)/2$, the equation (2.63) reduces to

$$\theta = \alpha_i L. \quad (2.64)$$

This condition, called critical coupling, implies that all input power is transferred to, and lost inside, the cavity under idealized circumstances. We will later assume that this condition holds, which is reasonable since any system design would generally strive to achieve maximum efficiency by satisfying it.

2.3 Parameter reduction

The Ikeda map (2.53), (2.58) as presented in the previous sections provides a complete description of the intracavity dynamics under the given assumptions, but contains many parameters to do so. To an experimentalist with specific values at hand this is not a problem, but since we seek to investigate the broader class of system represented by a range of values, this becomes a large space to search. We will therefore try to reduce the number of parameters, rendering the analysis more tractable.

Since the cavity dynamics are notably different depending on the sign of the group velocity dispersion β_2 , we factor it as $\beta_2 = s|\beta_2|$ with $s = 1$ indicating normal dispersion and $s = -1$ anomalous dispersion. With this addition, we can identify eight parameters α_i , s , $|\beta_2|$, γ , L , θ , δ and A_{in} in the Ikeda map. By introducing dimensionless, scaled versions of the variables z , t , A through

$$\xi = \frac{z}{z_0}, \quad \tau = \frac{t}{t_0}, \quad \psi = \frac{A}{A_0}, \quad (2.65)$$

we can exploit our free choice of scaling constants and pick

$$z_0 = L, \quad t_0 = \sqrt{\frac{|\beta_2|L}{2}}, \quad A_0 = \sqrt{\frac{1}{L\gamma}}, \quad (2.66)$$

resulting in the normalized Ikeda map

$$\frac{\partial \psi^m}{\partial \xi} = -\frac{\alpha_i L}{2} \psi^m - i s \frac{\partial^2 \psi^m}{\partial \tau^2} + i |\psi^m|^2 \psi^m, \quad (2.67)$$

$$\psi^{m+1}(0, \tau) = \sqrt{1 - \theta} e^{-i\delta} \psi^m(1, \tau) + \sqrt{\theta} \psi_{\text{in}}, \quad (2.68)$$

where

$$\psi_{\text{in}} = \sqrt{L\gamma} A_{\text{in}} \quad (2.69)$$

is the normalized pump power. The dependent variable ψ is here expressed in the scaled independent variables, with the longitudinal coordinate ξ in particular chosen so that the roundtrip distance equals unity.

To further reduce the parameter space we assume critical coupling (2.64), meaning $\theta = \alpha_i L = \alpha$. This reduces the Ikeda map to

$$\frac{\partial \psi^m}{\partial \xi} = -\frac{\alpha}{2} \psi^m - i s \frac{\partial^2 \psi^m}{\partial \tau^2} + i |\psi^m|^2 \psi^m, \quad (2.70)$$

$$\psi^{m+1}(0, \tau) = \sqrt{1 - \alpha} e^{-i\delta} \psi^m(1, \tau) + \sqrt{\alpha} \psi_{\text{in}}. \quad (2.71)$$

The normalized Ikeda map (2.70)–(2.71) now contains the three continuous parameters α , δ , ψ_{in} and one sign parameter s . By assuming a certain suitably high resonator finesse, which is related to the total cavity loss through $\mathcal{F} = \pi/\alpha$ [26], and make a choice of normal ($s = 1$) or anomalous

($s = -1$) dispersion, we are left with the detuning δ and normalized pump power ψ_{in} as the main system parameters. By examining solutions for different values of these we can effectively map the complete dynamics of any real world system characterized by the full Ikeda map with the same dispersion type and finesse. The specific choice of resonator finesse is discussed further in chapter 6.

To see that this is true, suppose we catalog solutions to the normalized system (2.70)–(2.71) for a two-dimensional range of parameter values δ, ψ_{in} . If we then translate the pump power of a real problem using (2.69), the corresponding solution of the normalized system can be retrieved. Finally, given the solution in terms of the scaled variables ξ, τ , and ψ , we recover their system specific analogue using (2.65) and (2.66). The influence of all parameters save two can this way be relegated to a scaling effect of the solution, which do not alter the essential dynamics. We chose to expose pump detuning and power as the influential parameters because they are most readily adjustable in an experimental setup.

Chapter 3

Lugiato-Lefever equation

If the length scales of the various dynamics affecting the pulse as it propagates through the cavity are considerably longer than the length of one roundtrip, and the boundary condition influence additionally is weak due to low coupling and detuning, we may conclude that the total pulse envelope rate of change on the time scale of individual roundtrips is small. Under these circumstances it would be desirable to express the continuous evolution of the pulse envelope on scales larger than one resonator roundtrip, but this is not possible with the Ikeda map formulation since each roundtrip is necessarily associated with the discontinuous influence of the boundary condition. We are therefore forced to evaluate the pulse evolution in steps smaller than the resonator circumference if we want to conduct numerical simulations.

An alternative model, called the Lugiato-Lefever equation [14], can be derived from the Ikeda map by distributing the presumed weak boundary effect over one roundtrip [16]. The result is a single driven, damped nonlinear Schrödinger equation allowing arbitrary step lengths, in addition to being more amenable to analytical treatment.

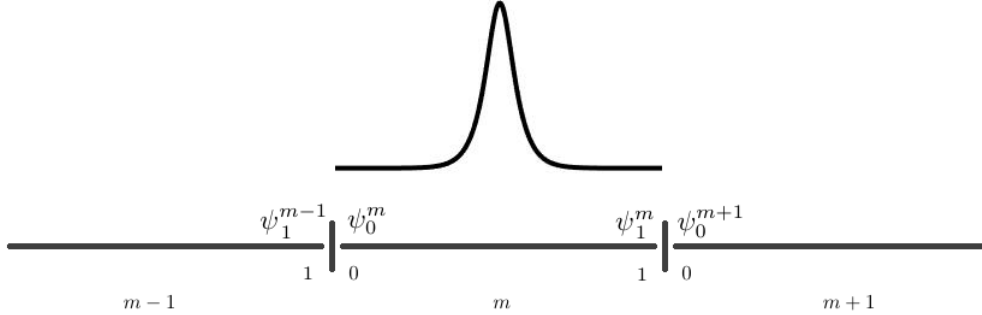


Figure 3.1: Several "unrolled" roundtrips of a propagating pulse.

Using the normalized Ikeda map (2.70)–(2.71), the Lugiato-Lefever equation is acquired by assuming that the weak boundary condition effect can be averaged over one roundtrip, and that the propagation over this distance alters the pulse very little. Adopting the notation $\psi_0^m = \psi^m(0, \tau)$, $\psi_1^m = \psi^m(1, \tau)$ (figure 3.1), we can write

$$\frac{\partial \psi}{\partial \eta} \approx \psi_0^{m+1} - \psi_0^m, \quad (3.1)$$

where we have defined the slow time η as a continuous extension of the discrete variable m normalized such that $\eta = 1$ corresponds to the roundtrip time t_R . In other words, $\partial \psi / \partial \eta$

is the envelope rate of change with respect to the roundtrip. In light of the presumed weak effects of propagation and boundary coupling on the field, we may view both as small, first order corrections. Expanding the boundary condition (2.71) in terms of first order corrections to the field ψ_1^m due to loss and detuning, we have

$$\psi_0^{m+1} \approx \left(1 - \frac{\alpha}{2} - i\delta\right) \psi_1^m + \sqrt{\alpha} \psi_{\text{in}}. \quad (3.2)$$

The field ψ_1^m can in turn also be considered as a correction to ψ_0^m due to propagation over one cavity length, and using (2.70) we get

$$\psi_1^m \approx \psi_0^m + \left. \frac{\partial \psi^m}{\partial \xi} \right|_{\xi=0} = \psi_0^m + \left(-\frac{\alpha}{2} \psi_0^m - is \left. \frac{\partial^2 \psi^m}{\partial \tau^2} \right|_{\xi=0} + i|\psi_0^m|^2 \psi_0^m \right). \quad (3.3)$$

Inserting (3.3) in (3.2) and ignoring higher order terms (coupling and propagation interaction), we get

$$\psi_0^{m+1} = (1 - \alpha - i\delta) \psi_0^m - is \left. \frac{\partial^2 \psi^m}{\partial \tau^2} \right|_{\xi=0} + i|\psi_0^m|^2 \psi_0^m + \sqrt{\alpha} \psi_{\text{in}}, \quad (3.4)$$

which in (3.1) finally yields the Lugiato-Lefever equation

$$\frac{\partial \psi}{\partial \eta} = -(\alpha + i\delta) \psi - is \frac{\partial^2 \psi}{\partial \tau^2} + i|\psi|^2 \psi + \sqrt{\alpha} \psi_{\text{in}}, \quad (3.5)$$

where again $\alpha = (\alpha_i L + \theta)/2$ is the total cavity loss and $\psi = \psi(\eta, \tau)$. In this equation, the pulse envelope is implicitly viewed from the same point ($\xi = 0$) in the resonator at all times, and the spatial variable ξ is instead replaced by the slow time η . The "normal" time τ is then referred to as the fast time, and carries the same interpretation as before, describing the envelope profile as it passes by our observation point while subject to the periodic boundary conditions. The slow time instead marks the pulse profile evolution over longer time scales, where the cavity dynamics are appreciable (figure 3.2). For more information on the LLE derivation, see [24][20].

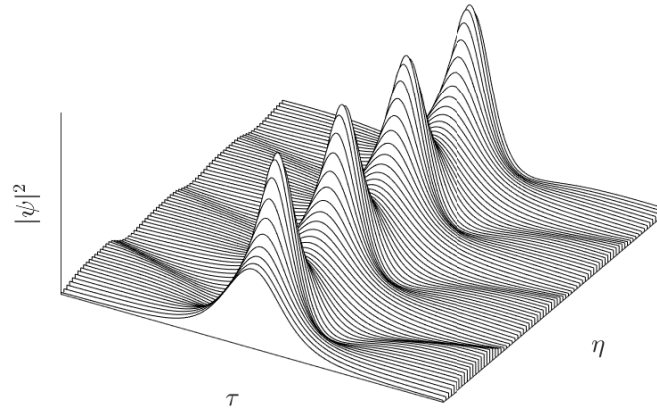


Figure 3.2: LLE breather soliton example. The fast time τ describes the pulse shape with periodic boundary conditions while the slow time η shows the pulse evolution.

Chapter 4

Analytical methods

The Ikeda map and Lugiato-Lefever equation have many interesting behaviors which can be gleaned without explicitly solving them. We will look at a few such cases which are instructive in predicting frequency comb dynamics.

In section 4.1, the exact CW solutions of the LLE potentially displaying bistability are acquired as a steady-state [14]. Section 4.2 conducts the same analysis for the Ikeda map and multistable CW solutions are explored [16]. The final section 4.3 shows the well-known phenomenon of modulational instability with respect to the LLE model [12], and the parameters expected to produce it.

4.1 Bistability

The simplest solutions we can hope to find in the LLE (3.5) are stationary, scaled versions of the continuous wave pump field ψ_{in} consisting of a single frequency component, having the suitably simple representation of a constant complex scalar (since the CW carrier wave is factored out). Existing in the balance between total cavity loss and pump driving averaged over one roundtrip, they are constant both between roundtrips (as measured by the slow time η) and in profile (as measured by the fast time τ). Accordingly, if such solutions exist, we expect to find them in the steady-state with all derivatives set to zero in (3.5). This results in

$$\left[\alpha + i \left(\delta - |\psi_{\text{cw}}|^2 \right) \right] \psi_{\text{cw}} = \sqrt{\alpha} \psi_{\text{in}}, \quad (4.1)$$

where ψ_{cw} is the CW solution. Forming the squared complex modulus of (4.1) provides a more interpretable equation in terms of field power (up to a normalizing factor),

$$\left[\alpha^2 + \left(\delta - |\psi_{\text{cw}}|^2 \right)^2 \right] |\psi_{\text{cw}}|^2 = \alpha |\psi_{\text{in}}|^2. \quad (4.2)$$

Equation (4.2) is a cubic polynomial in the power $|\psi_{\text{cw}}|^2$ and hence have either one or three real solutions. The influence of self-phase modulation – the intensity dependent phase contribution – is evident here as a shift of the effective detuning with increasing intracavity power. In the absence of this shift, (4.2) reduces to a Lorentzian function with exactly one solution $|\psi_{\text{cw}}|^2$ for all values of detuning δ , with resonance at $\delta = 0$ (left side in figure 1.2). With self-phase modulation, the resonance profile begins to tilt with increasing cavity power, and eventually we can start to observe detuning regions with three simultaneous solutions (figure 1.2 (c) where $\alpha = 3\text{e-}5$ and $|\psi_{\text{in}}|^2 = 1.2\text{e-}8$). The middle solution is however always unstable [14], so this region effectively contains two simultaneous solutions, referred to as the upper and lower branch, respectively.

4.2 Multistability

The Lugiato–Lefever equation (3.5) is well known for supporting bistable solutions as shown in the previous section, but being an approximation, it is relevant to conduct a similar analysis of the more general Ikeda map. The goal is again to find solutions which are replicated after each roundtrip in the cavity, and proceeding as before we assume a CW solution ψ_{cw} which is constant in profile (along the fast time τ). Unlike last time, however, we can't average the effects of cavity losses and pump forcing over one roundtrip and must provide a more detailed accounting of how the field profile evolves over this distance.

Starting by setting $\psi^{m+1}(0) = \psi^m(0) = \psi_{\text{cw}}(0)$, where the field is written only in terms of the spatial variable ξ , we get from (2.71)

$$\psi_{\text{cw}}(0) = \sqrt{1 - \alpha} e^{-i\delta} \psi_{\text{cw}}(1) + \sqrt{\alpha} \psi_{\text{in}}, \quad (4.3)$$

that is, whatever loss and phase the field has acquired after propagating one roundtrip must be undone by the boundary condition. Using that the field profile is constant at each spatial point ξ in the resonator, we can drop the time derivative in the pulse propagation equation (2.70), giving us

$$\frac{d\psi_{\text{cw}}}{d\xi} = -\frac{\alpha}{2} \psi_{\text{cw}} + i |\psi_{\text{cw}}|^2 \psi_{\text{cw}}, \quad (4.4)$$

which is an ordinary differential equation. We now wish to solve (4.4) for the field at $\psi_{\text{cw}}(1)$ given the initial field $\psi_{\text{cw}}(0)$ so that we can evaluate the corresponding term in (4.3). This can be accomplished by noting that the factor $|\psi_{\text{cw}}|^2$ has a simple behavior along ξ as it is unaffected by the nonlinear phase term, which allows us to substitute its solution directly,

$$\begin{aligned} \frac{d\psi_{\text{cw}}}{d\xi} &= -\frac{\alpha}{2} \psi_{\text{cw}} + i \left| \psi_{\text{cw}}(0) \exp\left(-\frac{\alpha}{2}\xi\right) \right|^2 \psi_{\text{cw}} \\ &= -\frac{\alpha}{2} \psi_{\text{cw}} + i |\psi_{\text{cw}}(0)|^2 \exp(-\alpha\xi) \psi_{\text{cw}}. \end{aligned} \quad (4.5)$$

This is a separable differential equation which can easily be solved. Using $\psi_{\text{cw}}(0)$ as the initial condition, we solve and then evaluate it at $\xi = 1$ to obtain

$$\psi_{\text{cw}}(1) = \psi_{\text{cw}}(0) \exp\left(-\frac{\alpha}{2} + i \frac{1 - e^{-\alpha}}{\alpha} |\psi_{\text{cw}}(0)|^2\right). \quad (4.6)$$

Inserting (4.6) in (4.3) and writing $\psi_{\text{cw}} = \psi_{\text{cw}}(0)$, we get

$$\psi_{\text{cw}} = \rho e^{i\phi} \psi_{\text{cw}} + \sqrt{\alpha} \psi_{\text{in}}, \quad (4.7)$$

where

$$\rho = \sqrt{1 - \alpha} \exp\left(-\frac{\alpha}{2}\right), \quad (4.8)$$

$$\phi = \frac{1 - e^{-\alpha}}{\alpha} |\psi_{\text{cw}}|^2 - \delta. \quad (4.9)$$

Like before, we can produce a more physically interpretable equation by taking the squared complex modulus,

$$\left|1 - \rho e^{i\phi}\right|^2 |\psi_{\text{cw}}|^2 = \alpha |\psi_{\text{in}}|^2, \quad (4.10)$$

which expanded using Euler's formula and simplified finally gives us

$$\left[(1 - \rho)^2 + 4\rho \sin^2(\phi/2)\right] |\psi_{\text{cw}}|^2 = \alpha |\psi_{\text{in}}|^2. \quad (4.11)$$

Using equation (4.11), we can determine the power $|\psi_{\text{cw}}|^2$ of possible CW solutions for different values of detuning δ . An example is shown graphically in figure 1.3 where $\alpha = 0.07$ and $|\psi_{\text{in}}|^2 = 1$. The effects of adjacent mode resonances can now be observed unlike in the bistable, LLE-based case which was contingent on small detuning. We see that for high enough cavity powers, neighboring resonance peaks tilt strongly enough as to overlap, creating regions with three or even more simultaneous stable solutions (keeping in mind that only the upper branch of each resonance contributes a stable solution). A similar analysis of Ikeda map multistability can be found in [16].

4.3 Modulational instability

The basic CW solutions found through (4.1) and (4.10) will only persist in the cavity if resistant to small perturbations. In this section, the linear stability of CW solutions produced by the Lugiato-Lefever equation is investigated. We start with the ansatz

$$\psi = \psi_{\text{cw}} + u + iv, \quad (4.12)$$

where ψ_{cw} is a constant CW solution satisfying (4.1), and u, v are small, real perturbations which are allowed to vary. We then insert (4.12) in the Lugiato-Lefever equation (3.5), ignore higher order terms in u, v , and subtract equation (4.1) to eliminate common terms to the non-perturbed CW solution. This results in

$$\frac{\partial u}{\partial \eta} + i \frac{\partial v}{\partial \eta} = -(\alpha + i\delta)(u + iv) - is \left(\frac{\partial^2 u}{\partial \tau^2} + i \frac{\partial^2 v}{\partial \tau^2} \right) + i |\psi_{\text{cw}}|^2 (3u + iv), \quad (4.13)$$

which is an evolution equation for the perturbations u and v linearized around the CW solution ψ_{cw} . We then reduce this equation to a linear ODE for each perturbation frequency by taking the Fourier transform with respect to the fast time,

$$\left(\frac{d\hat{u}}{d\eta} + i \frac{d\hat{v}}{d\eta} \right) = -(\alpha + i\delta)(\hat{u} + i\hat{v}) + is\omega^2(\hat{u} + i\hat{v}) + i |\psi_{\text{cw}}|^2 (3\hat{u} + i\hat{v}), \quad (4.14)$$

where \hat{u} , and \hat{v} are Fourier transforms of the perturbations. If we now separate the real and imaginary parts of (4.14), we get a coupled system of equations for the perturbations $\hat{w} = [\hat{u} \ \hat{v}]^T$,

$$\frac{d\hat{w}}{d\eta} = M\hat{w}, \quad (4.15)$$

where

$$M = \begin{bmatrix} -\alpha & \delta - s\omega^2 - |\psi_{\text{cw}}|^2 \\ -\delta + s\omega^2 + 3|\psi_{\text{cw}}|^2 & -\alpha \end{bmatrix}, \quad (4.16)$$

whose eigenvalues are found to be

$$\lambda = -\alpha \pm \sqrt{|\psi_{\text{cw}}|^4 - \left(\delta - s\omega^2 - 2|\psi_{\text{cw}}|^2 \right)^2}. \quad (4.17)$$

When the real part of one or both of these eigenvalues becomes positive, a perturbation oscillating at frequency ω starts growing exponentially. The initial perturbation will unavoidably be excited by vacuum fluctuations, and these regions are inherently unstable as a result. Examining the

gain spectrum by considering the largest real part of the two eigenvalues in (4.17) as a function of frequency ω , we find that two spectral sidebands start to grow symmetrically around the zero (pump) frequency as the intracavity power $|\psi_{\text{cw}}|^2$ increases above a threshold value. This is the parametric amplification corresponding to degenerate four-wave mixing, described in chapter 1, which initiates the potential self-organization of the system.

Examining (4.17), it is clear that this occurs when the second term in the radical becomes sufficiently small. In a straight waveguide such as an optical fiber, this is necessarily associated with anomalous group-velocity dispersion ($s = -1$) [13], but due to the extra degree of freedom afforded by the detuning parameter δ , MI becomes potentially accessible in a cavity resonator even with normal dispersion ($s = 1$) [28]. There are also other known mechanisms of instability present in the Ikeda map beyond MI which will not be treated in this work. The reader is directed to [16] for a stability analysis of the Ikeda map, and [24] for a similar analysis conducted here.

Chapter 5

Numerical methods

While a great deal of insight about the general features of the Ikeda map (2.70)–(2.71) and LLE (3.5) can be extracted through analytical methods such as those outlined in chapter 4, solutions are generally unavailable in closed form and must be generated numerically. Since both the Ikeda map and LLE essentially consist of propagation by means of nonlinear Schrödinger equation (NLSE), the majority of the effort will be focused on a space/time stepping scheme suited for

$$\frac{\partial \psi^m}{\partial \xi} = -\frac{\alpha}{2} \psi^m - is \frac{\partial^2 \psi^m}{\partial \tau^2} + i|\psi^m|^2 \psi^m, \quad (5.1)$$

$$\frac{\partial \psi}{\partial \eta} = -(\alpha + i\delta) \psi - is \frac{\partial^2 \psi}{\partial \tau^2} + i|\psi|^2 \psi + \sqrt{\alpha} \psi_{\text{in}}, \quad (5.2)$$

which is the Ikeda map NLSE and LLE NLSE, respectively.

Since the fast time τ enjoys naturally periodic boundary conditions due to covering one cavity roundtrip, we are invited to consider a spectral Fourier method [29] by evaluating the right hand side of (5.1) and (5.2) in the frequency domain for each step of the evolution variable. Providing both good performance using the Fast Fourier Transform (FFT) and very high accuracy with regard to the dispersion derivative terms (which can be traded for an increased integration step length), this is the ideal approach if applicable.

This approach is however hampered by the nonlinear terms which do not admit a simple representation in frequency space. Indeed, writing the field in terms of a Fourier basis of cavity modes

$$\psi(\tau) = \sum_k \hat{\psi}_k e^{i2\pi k\tau/t_R}, \quad (5.3)$$

where $\hat{\psi}_k$ is the amplitude of mode k and t_R is the roundtrip time, quickly reveals a coupled system of differential equations¹ upon insertion in (5.1) and (5.2), which is to be expected since the source of frequency comb formation originates in the interaction of frequency components.

In this chapter, the idea of operator splitting [25] is described which allows alternating steps with regard to the linear and nonlinear parts of (5.1) and (5.2) to be taken separately. This way, the linear part can make full use of spectral Fourier methods while the nonlinear part is simply evaluated in the time domain – a scheme known as the split-step Fourier method [13].

¹In a frequency description model, this system may be solved directly in terms of mode amplitudes [21].

5.1 Operator splitting

Consider the partial differential equation

$$\frac{\partial \psi}{\partial q} = (H(\psi) + L) \psi, \quad (5.4)$$

where $\psi(q, \tau)$ is acted on by the linear differential operator L and the nonlinear operator H which depends on ψ . The solution $\psi_1 = \psi(q_0 + h, \tau)$ given the initial condition $\psi_0 = \psi(q_0, \tau)$ is

$$\psi_1 \approx e^{h(H(\psi_0) + L)} \psi_0, \quad (5.5)$$

where h is small and the nonlinear operator is approximated as constant along h . In the special case when H and L commute, the effect of each can be calculated separately and sequentially as $\psi_1 = e^{hH} e^{hL} \psi_0$, which can be a significant simplification if $e^{hL} \psi$ and $e^{hH} \psi$ admit closed form solutions². The more typical scenario of interest, however, is that of noncommuting operators where this simplification is no longer exact. The idea of operator splitting, then, is to approximate

$$\psi_1 \approx e^{hH(\psi_{1/2})} e^{hL} \psi_0, \quad (5.6)$$

where $\psi_{1/2}$ is the intermediary result after applying the linear operator. This is known as first order operator splitting, and the numerical scheme for (5.4) consists of repeated and alternating application of the two exponentiated operators using an appropriately small step h . The validity of this approach can be explained using the Lie-Trotter product formula, which roughly states that $(e^{A/n} e^{B/n})^n$ converges to e^{A+B} in the limit of large n , where A and B are noncommuting operators.

A more accurate version of (5.6), known as second order or Strang splitting, is

$$\psi_1 \approx e^{\frac{h}{2}L} e^{hH(\psi_{1/2})} e^{\frac{h}{2}L} \psi_0. \quad (5.7)$$

This method is globally accurate to second order in h , whereas (5.6) is only accurate to first order, which can be verified by expanding the Taylor series of the exponentiated operators in (5.6), (5.7) and matching terms with that of (5.5) [25]. The numerical scheme using (5.7) is again the repeated application of the exponentiated operators to advance the solution in small steps of h ,

$$\psi_n = \left(e^{\frac{h}{2}L} e^{hH(\psi_{n-1/2})} e^{\frac{h}{2}L} \right) \dots \left(e^{\frac{h}{2}L} e^{hH(\psi_{1/2})} e^{\frac{h}{2}L} \right) \psi_0. \quad (5.8)$$

Written explicitly, it is easy to see that the bulk of $e^{\frac{h}{2}L}$ operators appear in pairs and can be merged to increase performance,

$$\psi_n = e^{-\frac{h}{2}L} \left(e^{hL} e^{hH(\psi_{n-1/2})} \right) \dots \left(e^{hL} e^{hH(\psi_{1/2})} \right) e^{\frac{h}{2}L} \psi_0, \quad (5.9)$$

where forward and backward half-steps still occur at the start and end to maintain equivalence with (5.8).

5.2 Split-step Fourier method

The split-step Fourier method makes use of the operator splitting technique to separate the linear and nonlinear parts of the propagation equations (5.1) and (5.2). In the following sections, the details pertaining to the split-step algorithm for each model is outlined.

²Even if this is not the case, it offers the flexibility of using different integration schemes for each operator which can be useful e.g. for stiff equations [30].

5.2.1 Ikeda map

Identifying the linear and nonlinear part of a discretized (5.1) in terms of operators, we have

$$L\psi^m(\xi, \tau) = \left(-\frac{\alpha}{2} - is\frac{\partial^2}{\partial \tau^2} \right) \psi^m(\xi, \tau), \quad (5.10)$$

$$H\psi^m(\xi, \tau) = \left(i|\psi^m(\xi, \tau)|^2 \right) \psi^m(\xi, \tau). \quad (5.11)$$

To be implemented as a numerical algorithm, we discretize the time and frequency variables according to $\tau_k = kt_R/K$ and $\omega_k = 2\pi k/t_R$ where $k \in \{-K/2 - 1, -K/2, \dots, K/2\}$ and where K is the number of frequency bins (each one representing a mode resonance, cf. (5.3)). This introduces a further source of error, which is discussed in chapter 6. The linear operator L can then be represented as a matrix, and in the frequency domain it is diagonal,

$$\hat{L} = -\frac{\alpha}{2} + is\omega_k^2. \quad (5.12)$$

This is used to evaluate the linear step,

$$\begin{aligned} \psi_{n+1/2}^m &= e^{hL} \psi_n^m \\ &= e^{hF^{-1}\hat{L}F} \psi_n^m \\ &= F^{-1} e^{h\hat{L}} F \psi_n^m, \end{aligned} \quad (5.13)$$

where again the subscript indicates the step number with the intermediary result after the linear operator written as a half step, and where F , F^{-1} are the discrete Fourier and inverse Fourier transforms with respect to the fast time τ_k . In other words, Fourier transform the field at ξ_n , multiply with the complex diagonal matrix $e^{h\hat{L}}$ and transform back to the time domain. The Fourier transforms can in principle be considered to be matrices, but in practice uses the Fast Fourier Transform algorithm.

The nonlinear step is performed directly in the time domain using the intermediate result $\psi_{n+1/2}^m$ produced by the linear step,

$$\begin{aligned} \psi_{n+1}^m &= e^{hH(\psi_{n+1/2}^m)} \psi_{n+1/2}^m \\ &= e^{ih|\psi_{n+1/2}^m|^2} \psi_{n+1/2}^m. \end{aligned} \quad (5.14)$$

By alternating linear (5.13) and nonlinear (5.14) steps according to (5.9), the pulse envelope ψ^m is propagated through the cavity. This process is repeated the number of steps $N = 1/h$ needed to traverse one cavity length (equal to unity in the normalized distance ξ), and is then complemented by the pump boundary condition

$$\psi_0^{m+1} = \sqrt{1 - \alpha} e^{-i\delta} \psi_N^m + \sqrt{\alpha} \psi_{\text{in}}, \quad (5.15)$$

completing one roundtrip through the cavity. The superscript m indicating the current roundtrip is used primarily for mathematical bookkeeping and is not actually needed to implement the algorithm. In practice, the boundary condition (5.15) is simply interleaved every N steps in what could otherwise be considered a single continuous waveguide. A MATLAB implementation of the Ikeda map split-step scheme can be found in appendix A.

5.2.2 Lugiato-Lefever equation

Due to the non-homogeneous constant term $\sqrt{\alpha}\psi_{\text{in}}$ in (5.2) corresponding to the averaged pump forcing, identification with (5.4) cannot be made directly. The constant term can however be accounted for as a particular solution in addition to the homogeneous solution in the linear step. Identifying the linear and nonlinear parts,

$$L\psi(\eta, \tau) = \left(-\alpha - i\delta - is\frac{\partial^2}{\partial \tau^2} \right) \psi(\eta, \tau), \quad (5.16)$$

$$H\psi(\eta, \tau) = \left(i|\psi(\eta, \tau)|^2 \right) \psi(\eta, \tau), \quad (5.17)$$

and using the frequency domain representation of L with the same discretization as the Ikeda model,

$$\widehat{L} = -\alpha - i\delta + is\omega_k^2, \quad (5.18)$$

the particular solution due to the accrued forcing over a step h can be calculated as

$$\begin{aligned} \psi_{p,n+1/2} &= \int_0^h e^{(h-s)L} \sqrt{\alpha}\psi_{\text{in}} \, ds \\ &= \int_0^h e^{(h-s)F^{-1}\widehat{L}F} \sqrt{\alpha}\psi_{\text{in}} \, ds \\ &= F^{-1} \left(\int_0^h e^{(h-s)\widehat{L}} \, ds \right) F \sqrt{\alpha}\psi_{\text{in}} \\ &= F^{-1} \left(\frac{e^{h\widehat{L}} - 1}{\widehat{L}} \right) F \sqrt{\alpha}\psi_{\text{in}}. \end{aligned} \quad (5.19)$$

This contribution is the same for every step and need only be evaluated once. The homogeneous solution produced by the initial value at the start of every step is acquired similarly to (5.13) as

$$\psi_{h,n+1/2} = F^{-1} e^{h\widehat{L}} F \psi_n. \quad (5.20)$$

Combining the two contributions, the linear step is then

$$\psi_{n+1/2} = F^{-1} \left(e^{h\widehat{L}} F \psi_n + \left(\frac{e^{h\widehat{L}} - 1}{\widehat{L}} \right) F \sqrt{\alpha}\psi_{\text{in}} \right). \quad (5.21)$$

The main difference to the evaluation of the Ikeda model linear step (5.13) is the addition of pump forcing in the frequency domain before transforming back to the time domain. Since ψ_{in} is a constant, this addition takes the form of a scaled Dirac delta function centered on zero, corresponding to the pump envelope frequency.

The nonlinear step is identical to that of the Ikeda map,

$$\psi_{n+1} = e^{ih|\psi_{n+1/2}|^2} \psi_{n+1/2}, \quad (5.22)$$

which, applied together with the linear step (5.21) in (5.9), furnishes the LLE split-step Fourier scheme. This time, no boundary effect needs to be interleaved since the averaged pump forcing is accounted for directly in the linear step. A MATLAB implementation of the LLE split-step scheme can be found in appendix B.

Chapter 6

Software design and simulations

This chapter documents the design, development and utilization of software used to conduct numerical simulations. The concrete code implementation is written in the proprietary MATLAB language, but since mostly generic procedural programming concepts such as functions and structures are referenced, it should be accessible to readers unfamiliar with the language.

6.1 Design process and goals

In this section, the code design phase and challenges encountered are described. The process is documented in its entirety, with later abandoned designs included. This is to motivate the decisions made for the final design, covered more thoroughly in the next section.

The main priorities guiding the code implementation were, in order:

1. Ensuring correctness of produced simulations.
2. Enabling parallel execution of several simulations.
3. Providing easy access to scheduling of new simulations and visualizations of past simulations.

Addressing the first priority, flaws in the correctness of results can appear with various degrees of subtlety. Most obvious are qualitatively erroneous behavior such as numerical instability or infeasible physical values. While not necessarily easy to rectify, these problems usually offer a clear direction to focus efforts. More difficult are problems regarding the accuracy of seemingly well-behaved simulations. A common strategy to validate simulations of Hamiltonian systems is to monitor conservation of total energy (assuming a symplectic integrator), but since the Kerr cavity is a dissipative system, this is not applicable.

To validate the simulations, both those produced by the Ikeda map and LLE, the following strategy was used. First, the results were compared with those of other code implementations [13] and broadly checked for the correct qualitative behavior (CW solutions, Turing patterns, chaos, solitons) in various parameter regions. Then, the agreement between analytical results produced in chapter 4, specifically the predicted power of CW solutions and MI threshold, were verified. The dynamics expected in each region were also confirmed, e.g. rough correlation between bistable regions and cavity solitons with initial conditions known to converge to specific solutions (hyperbolic secant approximations of solitons [16]). Finally, the effects of step length and discretization points were ascertained by testing different values and comparing results of otherwise equal systems. The conclusions of these tests are discussed in a later section.

Once the code was deemed fit for purpose, the second priority was to increase throughput by parallelizing the simulation process. This is especially relevant since the problem both requires a

large number of total systems to be simulated and is naturally parallel in nature. To accomplish this, the previous prototyping script code was adapted to a function accepting data structures representing individual systems, containing all relevant simulation parameters in addition to a circular buffer storing the field history. Each system could then be simulated piecemeal in chunks of roundtrips referred to as a series, where the number of roundtrips is chosen large enough to make function overhead costs negligible but small enough that one series is brief to the user. Each system was additionally allotted a budget, measuring the number of series it is currently set to execute. A collection of systems, referred to as a batch, could then be iterated over, exhausting the budget of each system through successive calls to the simulation function. Crucially, this loop is easily parallelized, which in MATLAB requires the Parallel Computing Toolbox. This significantly increased performance (a factor 4 – 6), and scales well with the addition of more CPU cores. It also offered the flexibility to increase the budget of systems which showed slow convergence.

Since the goal of increasing machine efficiency was essentially complete, focus shifted to the last priority which was the most challenging and exposed the human-in-the-loop nature of the workflow as a major bottleneck. The main input required from the user was classification of system states as either stationary (Turing patterns, solitons), fluctuating (breathers, chaos) or CW, budget renewal of selected systems and lastly system "forking", which uses the field of an existing system as an initial value and incrementally sweeps the detuning and pump power to designated new values.

The classification of states could be automated by measuring the field rate of change between successive series, curvature and distance from the local calculated CW solution. The batch could then be visualized by drawing the systems (figure 6.1). When a system range of interest had been identified by their ID numbers, they could be manipulated (increase budget, change noise, remove, fork, play, etc.) by calling appropriate functions accepting the batch and a range of ID numbers. This is where the aforementioned bottleneck appeared; the visualize-modify-

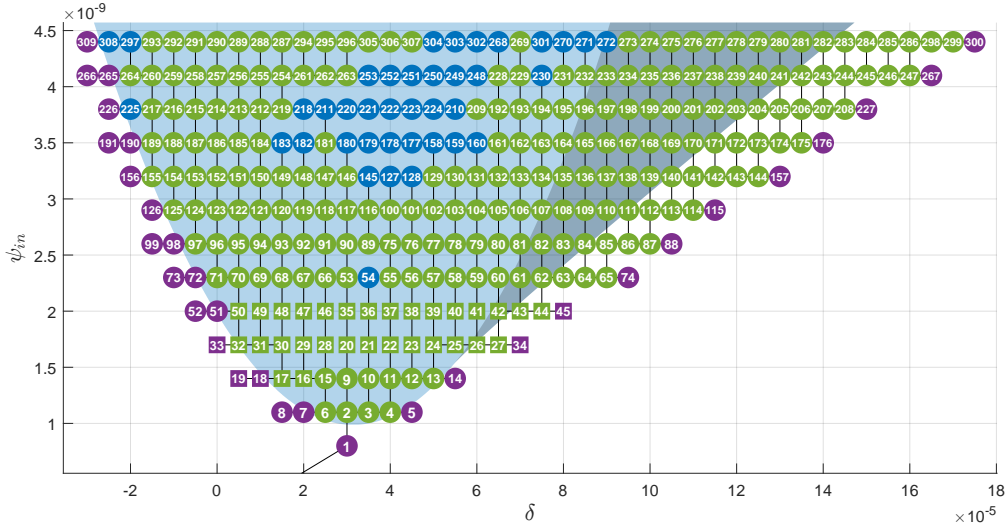


Figure 6.1: Example of early batch visualization. Each marker represents a system with detuning on the x-axis and pump power on the y-axis, and identified with an ID number. Colors designate state: stationary (green), fluctuating (blue) and CW (purple). Shapes indicate budget: zero (circle) and non-zero (square). The light blue background indicates regions with MI, and the darker region additionally indicate bistability.

simulate loop became dominated by the manual tracking of ID numbers. The original design was therefore partially abandoned in favor of a graphical user interface application, where systems could be manipulated directly from their graphical representation. The cost of the new design

was mitigated by the fact that many of the developed and tested functions could be reused as backend callbacks of the newly developed graphical frontend interface.

6.2 Kerr comb simulation application

This section gives a brief overview of the design and functionality of the final software used to conduct numerical simulations. It combines all tasks in one graphical user interface, which enables rapid creation, modification and visualization of individual systems, in addition to collective actions on selected groups of systems (figure 6.2). Groups of systems can also be viewed, sorted and selected from the table on the left side, where more properties are displayed.

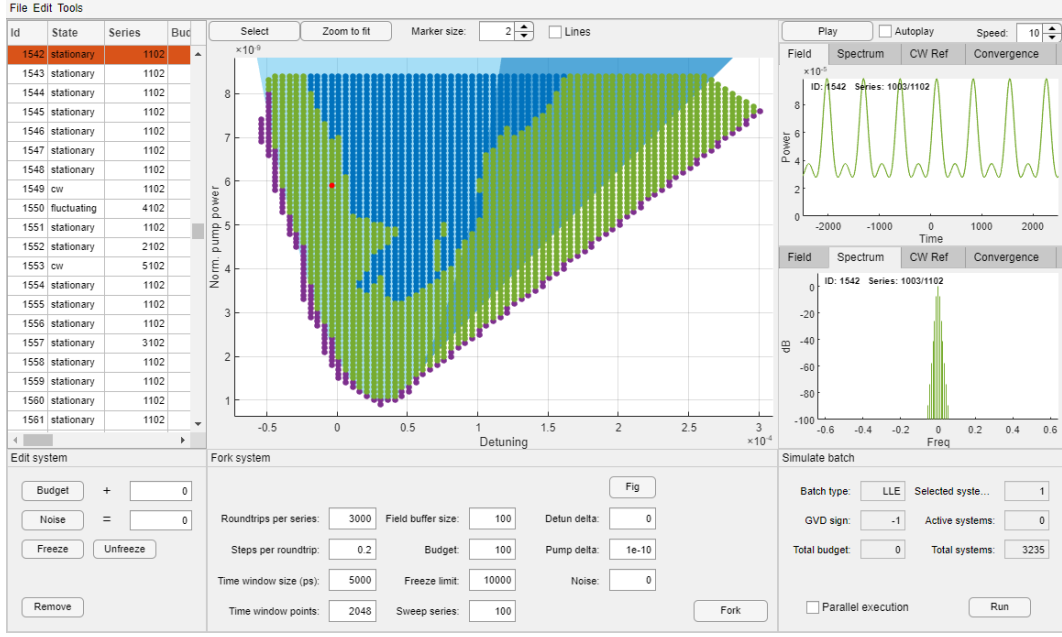


Figure 6.2: Simulation application v1.0. One system selected.

Additionally, a tool called autofork is accessible (figure 6.3), which selects systems of specified state on the batch boundary (adjustable with the shrink slider) and forks in selected directions. It also optionally renews the budget of systems with the highest variation between series. It then repeats this process in iterations until requested to cancel, allowing simulations to be scheduled with minimal user supervision. To prevent systems which are naturally time varying (chaos, breathers) from consuming the automatically renewed budget, each system "freezes" after a set number of series without changing state (indicated by a triangle marker), which disqualifies the system from receiving budget renewals unless manually reset. The application is open source and freely available [31] under the MIT license.

6.3 System and simulation parameters

According to the discussion on parameter reduction in chapter 2, a suitable choice of resonator finesse and group-velocity dispersion sign is needed to create a two-dimensional parameter space (pump frequency detuning and power). For the LLE, resonator finesse and by extension total cavity loss α can be eliminated using a different normalization [26], at the cost of a dissimilar parameter space to the Ikeda map and modified boundary conditions. It is unclear how the choice of finesse affects Ikeda map dynamics, but a value representative of a typical high quality optical cavity was deemed reasonable since the model is primarily of interest in the scenario of high

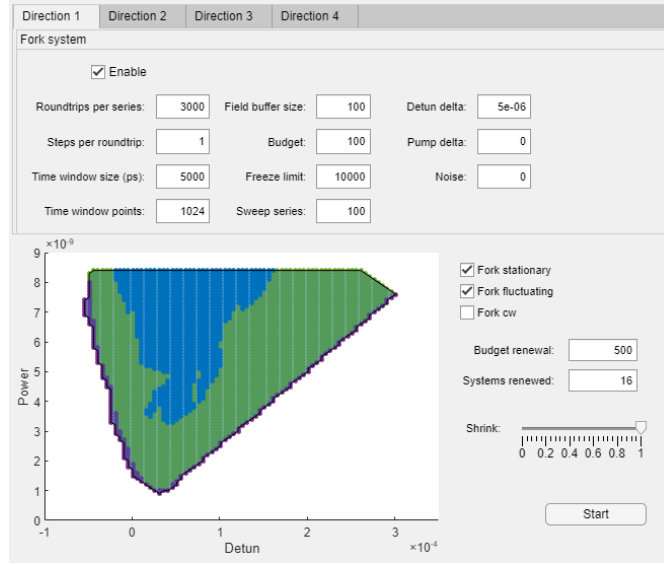


Figure 6.3: Autofork options.

intracavity power, which is more accessible in such a resonator. With this in mind, a finesse of $\mathcal{F} = 10^5$ was adopted, which is high but not unrealistic [26]. The group-velocity dispersion sign was constrained to the anomalous case $s = -1$ since this is the region typically associated with Kerr-comb dynamics such as bright cavity solitons. Normal dispersion $s = 1$ can also display non-trivial dynamics as discussed in chapter 4, but was considered a lower priority.

With the system parameters appropriately constrained, what remained to be determined were simulation parameters. It is not obvious how to choose these a priori and an iterative approach was employed to determine the effect on stability and solutions. It was found that the number of discretization points had little to no effect on either numerical stability or solutions above a certain value, which for the previously described system parameters was approximately 2^{11} . This is reasonable, as the power spectrum of the comb drops off rapidly in accordance with the quasi-monochromatic field assumption, and adding more frequency bins (mode resonance) therefore yield diminishing returns after a certain point. As is evident from the time and frequency discretization used in chapter 5, the roundtrip time t_R also plays an important role, and was essentially considered a simulation parameter even though it is technically a system parameter. To justify this we note that, from a frequency domain perspective, the effect of lowering t_R is simply to increase the comb teeth spacing, which coupled with the fact that t_R does not appear in either the normalized Ikeda map or LLE means that it plays a minor role on a theoretical level.

The step length was more consequential in terms of numerical stability, but also produced very little difference in terms of solutions once stability was reached in both models. Unlike the number of discretization points, the stability threshold was dependent on intracavity power, requiring more steps per roundtrip for larger power. The strategy therefore became to use as few steps per roundtrip as possible while avoiding instability. For the LLE, which admits fractional steps per roundtrip, this number ranged between 0.1 and 0.5 in the low intracavity power region (approximately below 10^{-8}), but could likely have been taken even lower for the regions of low power. The Ikeda map required between 1 and 2 in the same region, and often far exceeded 2000 in the high-power region (approximately above 10^{-4}).

Finally, the remaining simulation parameters exclusive to the software developed are tuned mainly to achieve good performance and to provide flexibility. These are presented below, with short pointers on their intended use.

- Number of roundtrips per series. Define in relation to the number of steps per roundtrip and machine performance to make budget units (series) an appropriate size. Since the field buffer stores snapshots separated by one series, it must also be picked to balance duration and resolution of dynamics during playback.
- Field buffer size. Use a value which balances field history length and data size (the circular field buffer constitutes the bulk of system storage).
- Budget. Initial budget of system(s).
- Freeze limit. Use a value large enough that most systems which can converge to a stationary state has time to do so, but small enough that inherently fluctuating systems do not consume too much time.
- Sweep series. The number of series in the budget devoted to sweeping a system between its initial and final point in detuning / power space. Balance performance with stability.
- Detuning and power range. The initial and final parameter points if a new system is created. Can be picked graphically via the "fig" buttons.
- Detuning and power delta. The parameter change through sweeping if a system is forked. Can be picked graphically via the "fig" button.
- Noise. Noise added to the field of the system in each series which is uniformly distributed up to the supplied value. Use if a continuous addition of noise is required beyond initial noise, either to excite patterns from a CW state or to test stability of existing patterns.

The resonator finesse, GVD type and various other auxiliary parameters are chosen when a new batch is created and applies for all systems.

6.4 Workflow

This section describes the general workflow used in the previously described software to expand the explored parameter space of a batch. The work can roughly be divided into two stages. First, a system in the state which is to be studied is generated. This can be done either by creating a system initialized with a field close to the desired state (e.g. solitons), or with noise and let the system self-organize to a Turing pattern. Both of these approaches require the parameters to support the desired dynamics, and for single soliton states, Gaussian and hyperbolic secant approximations are available, with the parameters of the latter automatically provided based on the selected detuning and power.

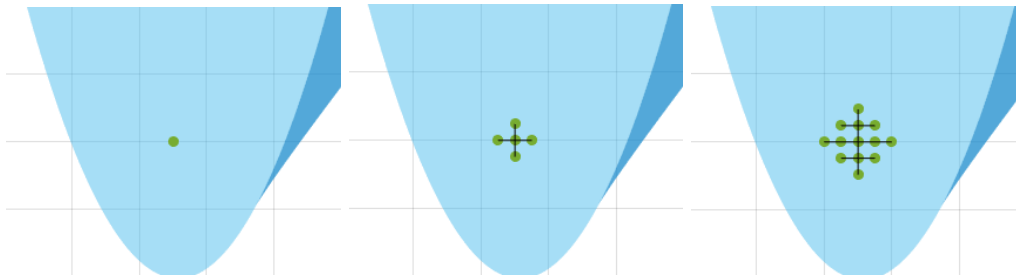


Figure 6.4: Forking process

When a stable solution has been generated, the second task is to sweep or "fork" the system to a new detuning and power point. Provided the sweep is not too aggressive, and the new point supports the same dynamics, the solution remains stable. This process is then repeated, exploring the parameter space through a tree structure (figure 6.4).

Chapter 7

Results and discussion

In this chapter, the results of conducted parameter sweeps are presented, along with analysis and comments. The shaded background corresponds to MI (light blue) and bistability (dark blue). All results are with respect to the normalized coordinates (2.65), the cavity finesse was fixed at $\mathcal{F} = 10^5$ and the GVD was anomalous $s = -1$.

7.1 Low-power region

Dynamics in the low-power regime (approximately $|\psi|^2 < 1e^{-8}$ for the present work) for both the LLE and Ikeda map are presented in figure (7.1).

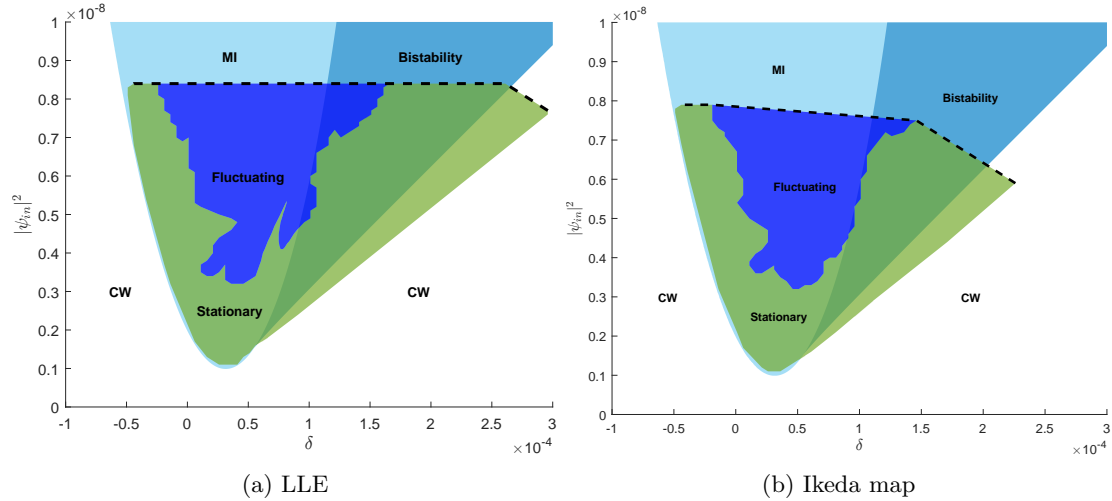


Figure 7.1: Low-power parameter region for the LLE (a) and Ikeda map (b). The stationary regions contain patterns which do not change between roundtrips, such as Turing patterns and solitons. The fluctuating regions conversely contain non-stationary dynamics such as breathers and chaos. The background shading indicates predicted regions with MI and bistability, where bistable regions also possess MI. The upper dotted lines represent the frontier of explored parameters and have no further significance.

Both images were generated by initializing a system with noise near the lowest possible pump power predicted to contain MI and forking the emerging stationary pattern in all directions. The boundaries between dynamical regimes were then sampled to delineate the regions. Fewer systems were simulated in the Ikeda map owing to the larger computational time required, and the interior of the fluctuating region was partially unexplored (see full data in appendix C).

While the initial system state for both models was a Turing pattern, it transitioned over to solitons in regions near bistability. The transition was generally gradual with the two dynamical regimes overlapping¹. Some patterns were topologically compatible (same number of peaks) with its new parameters and converged quickly (a few hundred thousand roundtrips). Others were not, however, and gradually destabilized to then reorganize into another pattern, requiring more time. A few systems near the boundaries of dynamical regimes displayed extremely slow convergence, routinely exceeding tens of millions of roundtrips with little progress. This was especially true for systems only barely displaying MI.

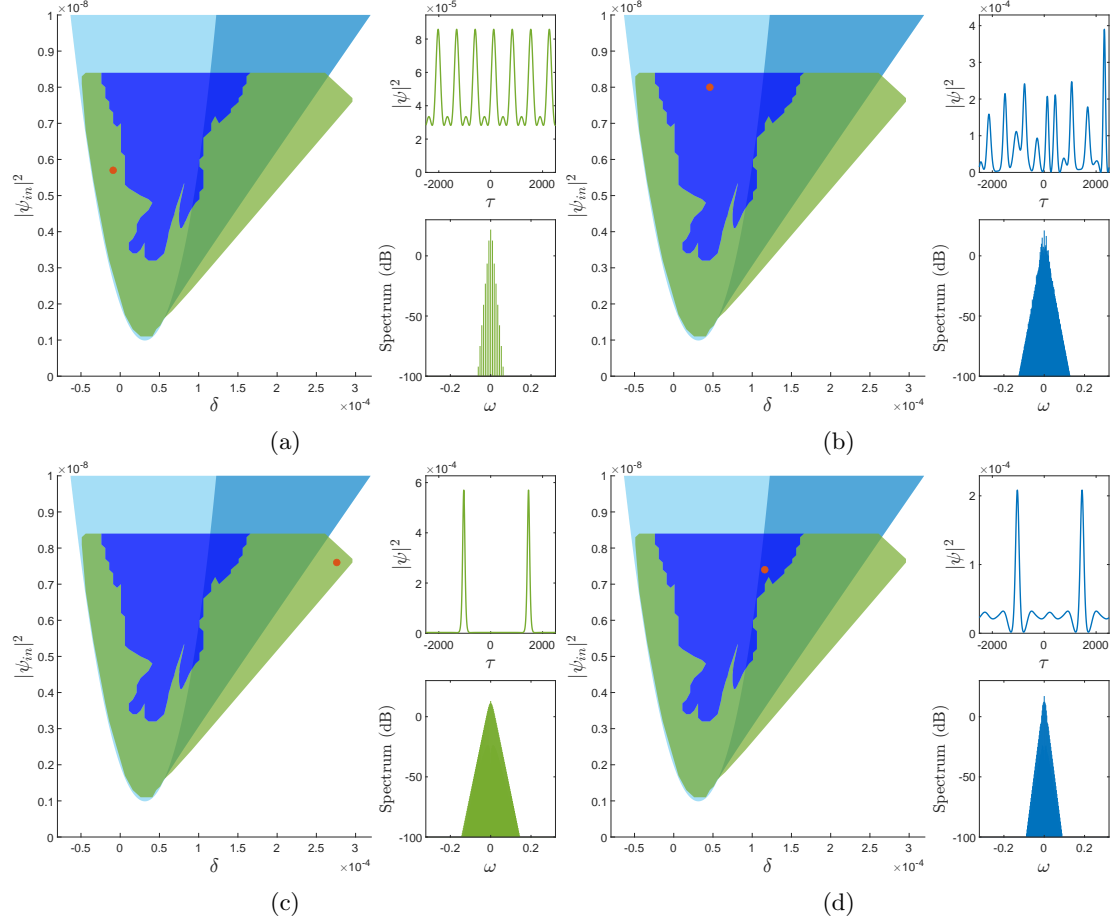


Figure 7.2: Sampled systems from the LLE batch. Dynamics displayed are (a) Turing pattern, (b) chaos, (c) stationary solitons and (d) breathing solitons.

Other dynamics of note beyond Turing patterns and solitons were breathing patterns, where a previously stationary Turing pattern or soliton(s) underwent a Hopf bifurcation and started to oscillate periodically. These generally occurred near the boundary of stable patterns. Lastly, there were chaotic regimes which had lost all time domain structure. Some sampled systems from each batch are displayed in figure 7.2 and figure 7.3.

¹Here we define a localized pattern as one that can be removed (returned to the stable CW background) without noticeably affecting other patterns coexisting in the cavity.

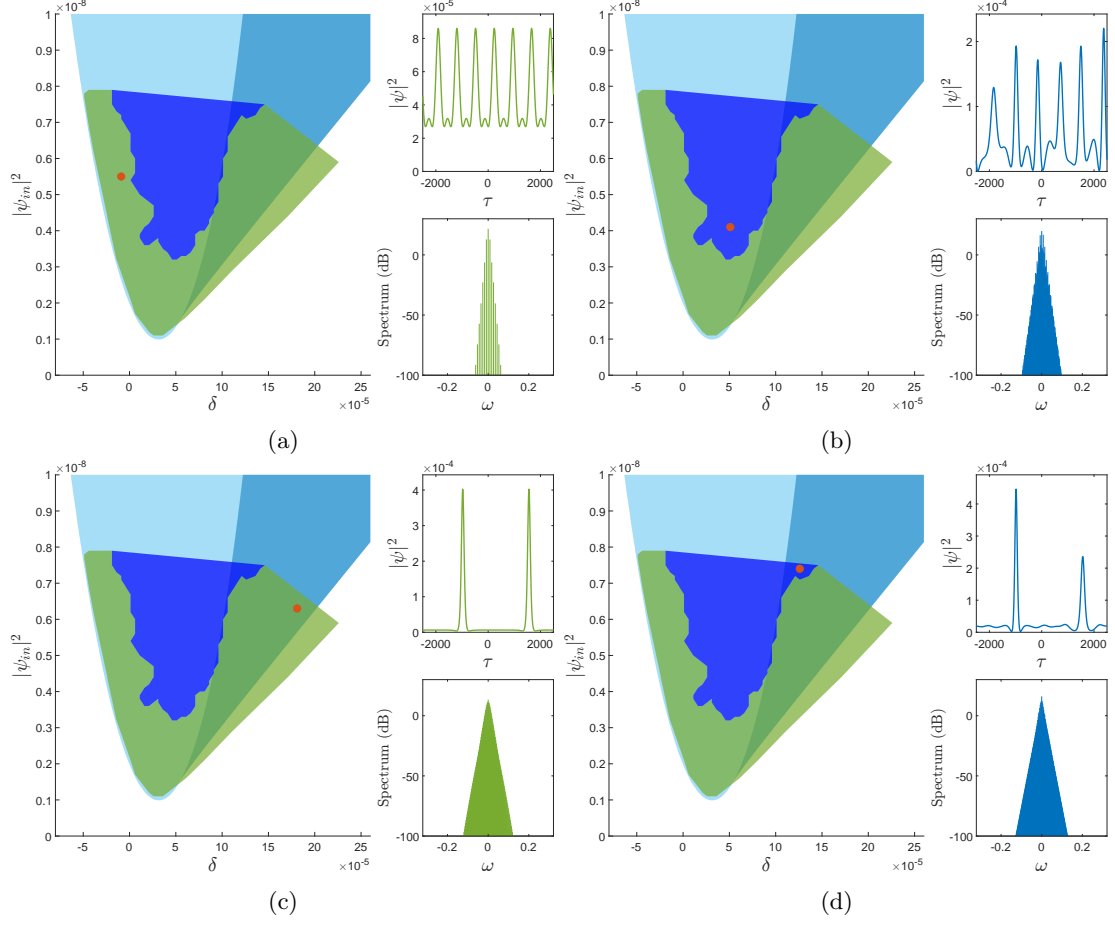


Figure 7.3: Sampled systems from the low-power Ikeda batch. Dynamics displayed are (a) Turing pattern, (b) chaos, (c) stationary solitons and (d) breathing solitons. The asymmetric breathers are not unique to the Ikeda map and were found also in the LLE.

The agreement between predicted regions with MI and dynamics other than trivial CW solutions is excellent in both models for the low-power region. Further, the two models broadly behave similarly, which is not surprising since the LLE is a good approximation in regions of low power. The boundary delimiting stationary and fluctuating systems display some difference between models, with the LLE looking more intricate in this respect. One notable example is an incursion of stationary Turing patterns into the fluctuating regime found in the LLE, which could be an Arnold tongue [32]. This was seemingly not mirrored in the Ikeda map (figure 7.4), which might indicate that such peculiarities in the boundary could be an artifact of the LLE approximation. Both phase diagrams show good agreement with previous theoretical and experimental investigations [16][33][34][15][35]

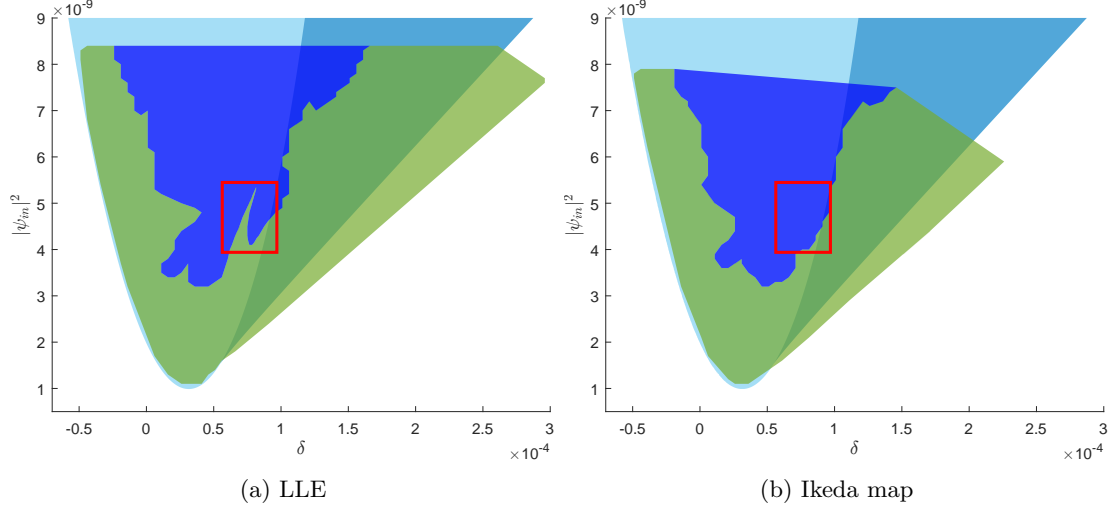


Figure 7.4: Incursion of stationary dynamics in otherwise fluctuating region found in the LLE.

An additional batch was also simulated with a single soliton excitation as an initial value. This was to investigate the boundary between Turing patterns and solitons more clearly, since a transition from the former, as encountered in the previous batch, generally resulted in multi-soliton complexes (several coexisting solitons, figure 7.2 (c)), which could conversely transition back to Turing patterns. This process was gradual, which made the boundary unclear. A single soliton could not undergo a transition to a Turing pattern, however, and instead commenced a breathing behavior (or collapsed to a CW solution) immediately when moved outside the soliton boundary, making it sharp (figure 7.5).

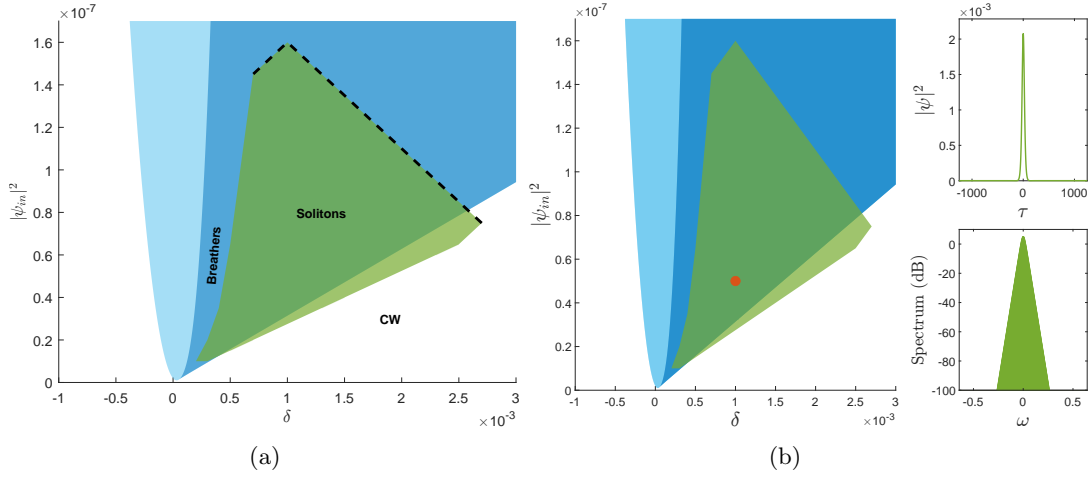


Figure 7.5: Soliton region of the LLE.

7.2 High-power region

For the high-power region (pump power above approximately 10^{-4} for the parameters used) only the Ikeda map was examined since this region is generally far outside the range of validity used in the LLE approximation [16]. Figure 7.6 shows the parameter regions capable of supporting super cavity solitons of the first excited state, roughly corresponding to regions with tristability. The first system was initialized with a hyperbolic secant approximation [16] and then forked through parameter values.

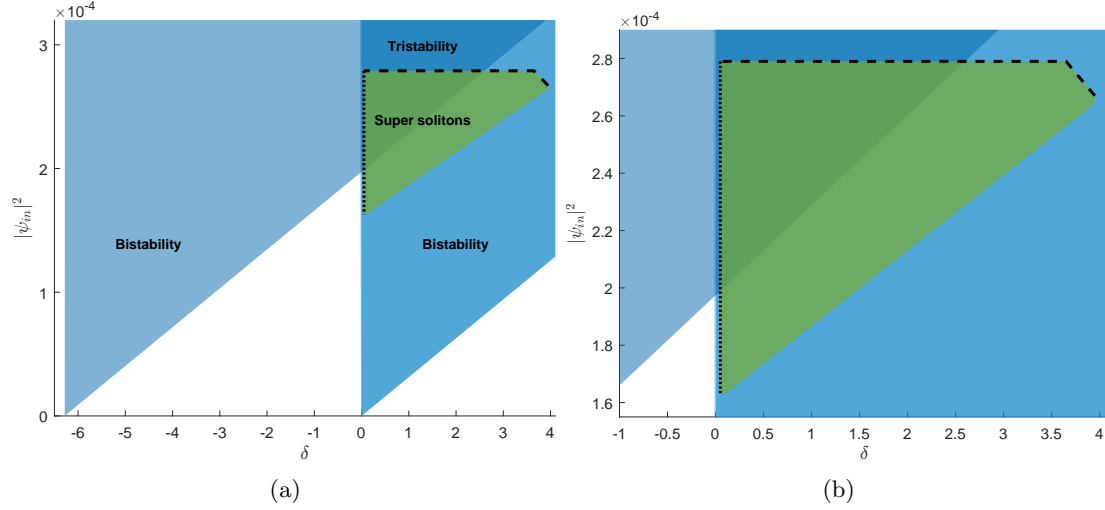


Figure 7.6: Ikeda batch in the high energy regime. Bistability from the adjacent mode resonance is displayed as an additional layer of blue shading, with tristability in the overlapping region. The dashed line is again the frontier of the explored region, but the dotted line marks a potential stability boundary.

Due to the high intracavity power, this set of simulations required substantially more steps per roundtrip (around 2000). This implied much lower system throughput and limited the volume of parameter space which could be explored. This was somewhat ameliorated by the quick convergence of soliton solutions inside their basin of attraction. The strategy was therefore to maximize the sweep step length without falling outside the basin. One potential boundary encountered indicated with a dotted line in figure 7.6 occurred at the transition out of the native mode bistability, where the soliton commenced an irregular beating. This was attributed to the stable CW background on which the soliton rests becoming inaccessible as the lower branch of the native mode resonance ends. Tests in this region indicated that the soliton might recover from the irregular beating with time, but a general conclusion is unavailable. The other boundary encountered for high detuning was similar to the one found for "regular" solitons, where the peak power falls off its local multistability curve.

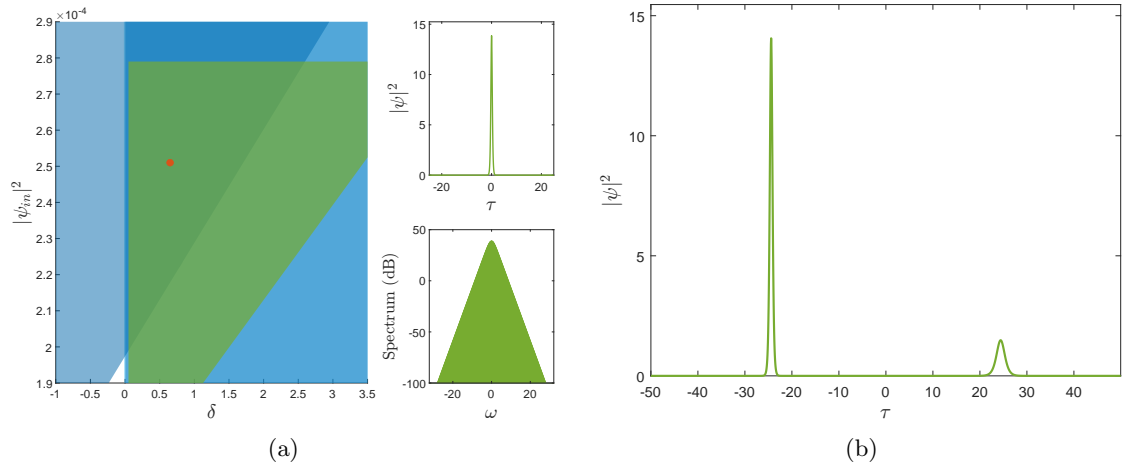


Figure 7.7: Two examples of Ikeda map systems, where (a) is a sampled system from the high-energy batch in figure 7.6 and (b) is a system with a super soliton and an ordinary soliton coexisting.

A sampled system from the batch is presented in figure 7.7 (a), and a system with both a super cavity soliton and an ordinary soliton coexisting is found in (b), which has been observed experimentally [17]. It is seen that the super cavity soliton is much narrower than its ordinary counterpart, and therefore has a significantly wider comb spectrum.

7.3 Validity of results

Each of the generated phase diagrams presented in this chapter must be interpreted with some degree of uncertainty. The finite simulation time allotted to each system leaves the possibility open for misclassification of parameter regions; some seemingly noteworthy system dynamics suddenly returned to their expected behavior after drastically increasing their simulation time. This is especially true for transitions between stationary and fluctuating states, which often displayed such slow convergence that they seemingly depended on what state they originated from. This was likely not a sign of hysteresis with coexistence of stationary and fluctuating states at a parameter point, and they would likely converge given enough time.

It is likely that the boundaries of both the LLE and Ikeda map reveal even more intricate structure if sampled more finely. The previously mentioned stationary patch in the otherwise fluctuating region was only discovered after a few coarsely sampled systems happened to land in it, after which it was sampled further.

Chapter 8

Conclusions

The link between parameters of a general optical Kerr cavity and its dynamics with regard to frequency comb generation was explored in this work. Mathematical models were reviewed and used to model the intracavity field of a general optical Kerr cavity, which were then probed analytically. This narrowed the parameter search and provided a reference point in numerical simulations, which were conducted using the split-step Fourier method in a custom simulation package. The main result of note was the parameter region supporting super cavity solitons, which was found to exhibit a strong dependence on multistability. Another potentially notable result was the intricate boundary separating stationary and fluctuating systems in the low-power region, where the LLE was found to possess complexity not present in the Ikeda map.

The produced parameter maps in the low-power region essentially satisfy the stated goals of comparing the models, but are arguably incomplete and would have benefited from covering a larger parameter range. Especially high enough pump powers to produce a noticeable disagreement between the LLE based MI region and corresponding Ikeda map instability would have been of interest to more clearly elucidate the point of divergence between the models. It could also be beneficial to conduct an Ikeda soliton boundary analysis similar to the LLE one. Another interesting (though time intensive) task would be to conduct parameter sweeps for different cavity finesse and examine how the dynamical landscape changes in the Ikeda map. Lastly, the phenomena of dark cavity solitons associated with normal GVD was left unexplored. It is the hope of the author that the software produced will be of use to anyone interested in conducting further work in simulating optical Kerr combs.

Appendix A

Ikeda map code

The MATLAB implementation of the split-step Fourier integration scheme for the Ikeda map is presented here. The variable "sys" is a structure representing a system and its parameters. Specifically, it contains the simulation parameters N (number of steps per roundtrip), R (number of roundtrips per series), T (time window size, equal to the roundtrip time t_R) and nT (number of time window points), in addition to system parameters.

```
function sys = split_step_Ikeda(sys)
% Execute one series of Ikeda map roundtrips using the split step
  scheme.

  dz = 1/sys.N; % Step size
  omega = fftshift((2*pi/sys.T)*(-sys.nT/2:sys.nT/2-1)); %
    Frequency grid

  % Retrieve current field
  psi = sys.field_buffer(mod(sys.series - 1, sys.buffer_size) +
    1, :);

  % Update parameter sweeps
  sys.detun = interp1([1 sys.sweep_series], ...
    [sys.detun_start sys.detun_end], ...
    sys.series, 'linear', sys.detun_end);
  sys.power = interp1([1 sys.sweep_series], ...
    [sys.power_start sys.power_end], ...
    sys.series, 'linear', sys.power_end);

  D = exp((-sys.alpha/2 + 1i*sys.s*omega.^2)*dz);

  % Add noise
  psi = psi + sys.noise_gen(sys.noise(end));

  % Linear half-step
  psi = ifft(fft(psi).*sqrt(D));

  for r = 1:sys.R
    for n = 1:sys.N
```

```

        % Nonlinear step
        psi = psi.*exp(1i*abs(psi).^2*dz);

        % Linear step
        psi = ifft(fft(psi).*D);
    end

    % Boundary condition
    psi = sqrt(1 - sys.alpha)*exp(-1i*sys.detun)*psi + ...
        sqrt(sys.alpha*sys.power);
end

% Inverse linear half-step
psi = ifft(fft(psi).*1./sqrt(D));

% Store field
sys.series = sys.series + 1;
sys.field_buffer(mod(sys.series - 1, sys.buffer_size) + 1, :)
    = psi;
end

```

Appendix B

Lugiato-Lefever equation code

The MATLAB implementation of the split-step Fourier integration scheme for the Ikeda map is presented here. The variable "sys" is a structure representing a system and its parameters. Specifically, it contains the simulation parameters N (number of steps per roundtrip), R (number of roundtrips per series), T (time window size, equal to the roundtrip time t_R) and nT (number of time window points), in addition to system parameters.

```
function sys = split_step_LLE(sys)
% Execute one series of LLE roundtrips using the split step scheme
.

dR = 1/sys.N;           % Step size
Q = round(sys.R/dR);    % Number of steps in series
omega = fftshift((2*pi/sys.T)*(-sys.nT/2:sys.nT/2-1)); %
    Frequency grid

% Retrieve current field
psi = sys.field_buffer(mod(sys.series - 1, sys.buffer_size) +
    1, :);

% Update parameter sweeps
sys.detun = interp1([1 sys.sweep_series], ...
    [sys.detun_start sys.detun_end], ...
    sys.series, 'linear', sys.detun_end);
sys.power = interp1([1 sys.sweep_series], ...
    [sys.power_start sys.power_end], ...
    sys.series, 'linear', sys.power_end);

P_hat = fft(sqrt(sys.power)*ones(1, sys.nT)); % Frequency
    domain power
D1 = -sys.alpha - 1i*sys.detun + 1i*sys.s*omega.^2;
D2 = exp(D1*dR);

% Add noise
psi = psi + sys.noise_gen(sys.noise(end));

% Initial linear half-step
```

```

psi = ifft(fft(psi).*sqrt(D2) + ...
           (sqrt(sys.alpha)*P_hat./D1).*(sqrt(D2) - 1));

for q = 1:Q
    % Nonlinear step
    psi = psi.*exp(1i*dR*abs(psi).^2);

    % Linear step
    psi = ifft(fft(psi).*D2 + (sqrt(sys.alpha)*P_hat./D1).*(D2
        - 1));
end

% Inverse linear half-step
psi = ifft(fft(psi).*1./sqrt(D2) + ...
           (sqrt(sys.alpha)*P_hat./D1).*(1./sqrt(D2) - 1));

% Store field
sys.series = sys.series + 1;
sys.field_buffer(mod(sys.series - 1, sys.buffer_size) + 1, :)
    = psi;
end

```

Appendix C

Simulation data

Data from conducted parameter sweeps are presented in this section. Green markers indicate stationary systems, blue fluctuating and purple CW states.

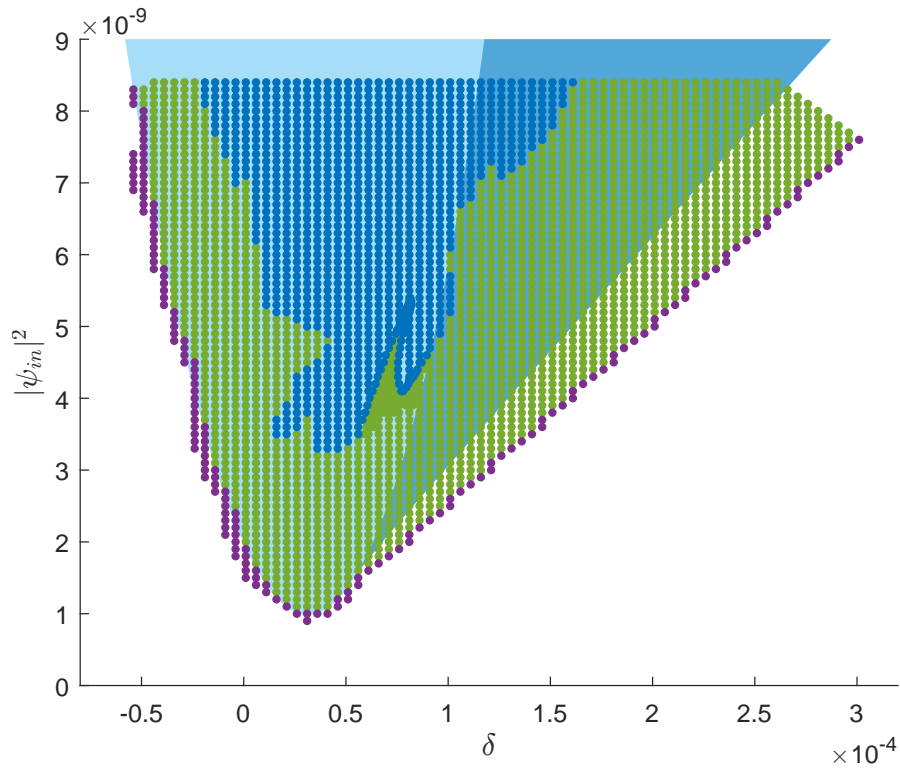


Figure C.1: Low-power region of the LLE.

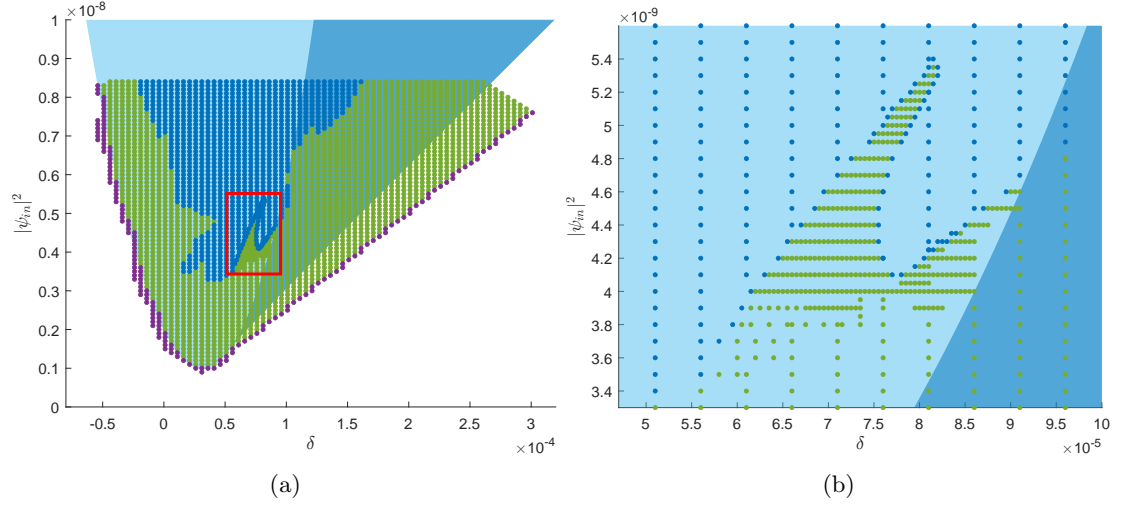


Figure C.2: Magnified view of a region in the LLE which was sampled with a higher number of systems.

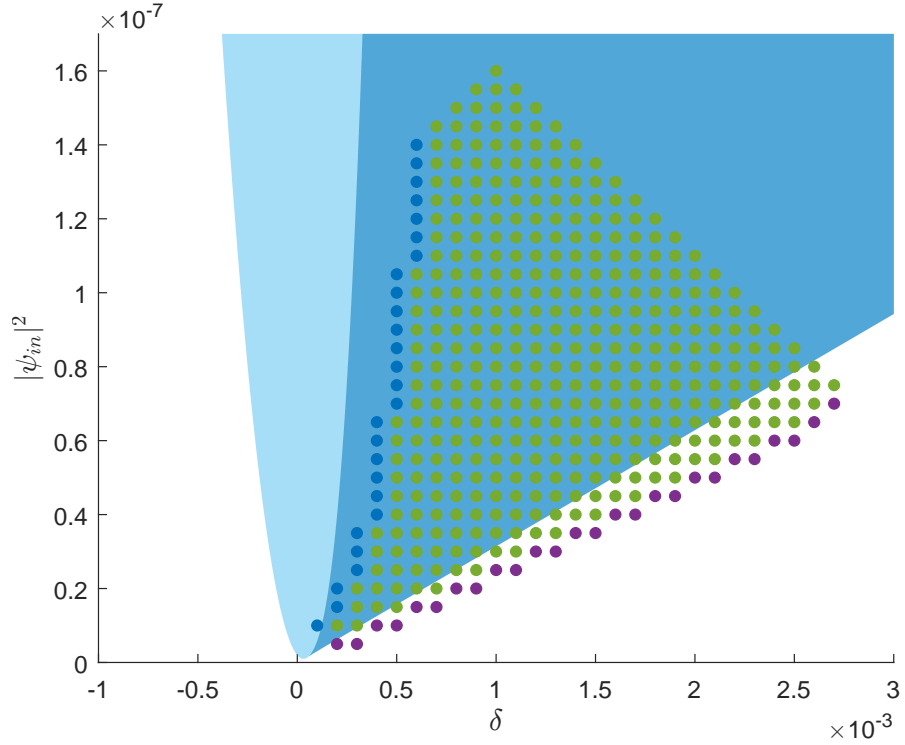


Figure C.3: Solitons in the LLE.

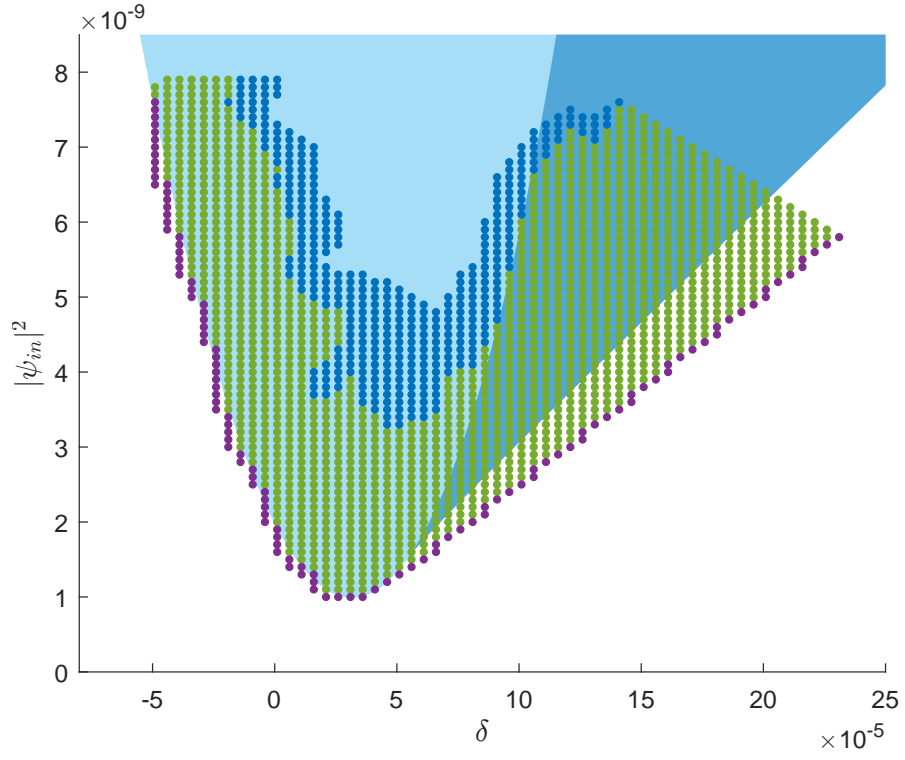


Figure C.4: Low-power region in the Ikeda map.

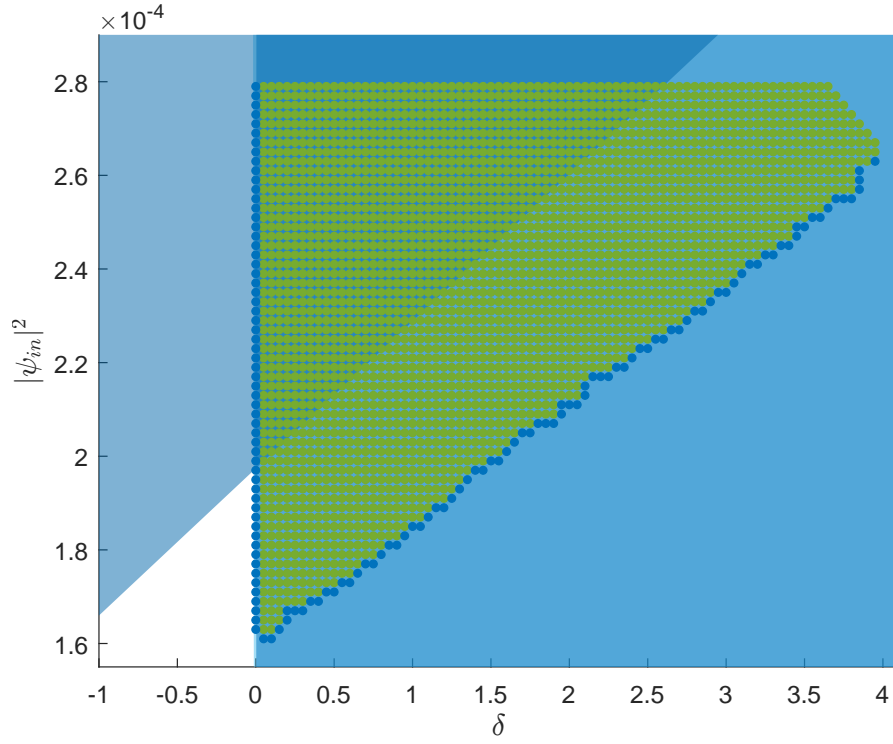


Figure C.5: High-power region in the Ikeda map with super cavity solitons.

Bibliography

- [1] Scott A Diddams et al. “An optical clock based on a single trapped 199Hg^+ ion”. In: *Science* 293.5531 (2001), pp. 825–828.
- [2] Pablo Marin-Palomo et al. “Microresonator-based solitons for massively parallel coherent optical communications”. In: *Nature* 546.7657 (2017), pp. 274–279.
- [3] Myoung-Gyun Suh et al. “Searching for exoplanets using a microresonator astrocomb”. In: *Nature Photonics* 13.1 (2019), pp. 25–30.
- [4] Tobias J Kippenberg, Ronald Holzwarth, and Scott A Diddams. “Microresonator-based optical frequency combs”. In: *Science* 332.6029 (2011), pp. 555–559.
- [5] Steven Cundiff, Jun Ye, and John Hall. “Rulers of light”. In: *Scientific American* 298.4 (2008), pp. 74–81.
- [6] Pascal Del’Haye et al. “Full stabilization of a microresonator-based optical frequency comb”. In: *Physical Review Letters* 101.5 (2008), p. 053903.
- [7] Pascal Del’Haye et al. “Optical frequency comb generation from a monolithic microresonator”. In: *Nature* 450.7173 (2007), pp. 1214–1217.
- [8] Andrey B Matsko and Vladimir S Ilchenko. “Optical resonators with whispering-gallery modes-part I: basics”. In: *IEEE Journal of Selected Topics in Quantum Electronics* 12.1 (2006), pp. 3–14.
- [9] Robert W Boyd. *Nonlinear Optics*. Academic press, 2002.
- [10] Masataka Nakazawa, Kazunori Suzuki, and Hermann A Haus. “Modulational instability oscillation in nonlinear dispersive ring cavity”. In: *Physical Review A* 38.10 (1988), p. 5193.
- [11] Marc Haelterman, Stefano Trillo, and Stefan Wabnitz. “Dissipative modulation instability in a nonlinear dispersive ring cavity”. In: *Optics Communications* 91.5-6 (1992), pp. 401–407.
- [12] Vladimir E Zakharov and Lev A Ostrovsky. “Modulation instability: the beginning”. In: *Physica D: Nonlinear Phenomena* 238.5 (2009), pp. 540–548.
- [13] Govind P Agrawal. *Nonlinear Fiber Optics*. Springer, 2000.
- [14] Luigi A Lugiato and René Lefever. “Spatial dissipative structures in passive optical systems”. In: *Physical Review Letters* 58.21 (1987), p. 2209.
- [15] Pedro Parra-Rivas et al. “Dynamics of localized and patterned structures in the Lugiato-Lefever equation determine the stability and shape of optical frequency combs”. In: *Physical Review A* 89.4 (2014), p. 043813.
- [16] Tobias Hansson and Stefan Wabnitz. “Frequency comb generation beyond the Lugiato-Lefever equation: multi-stability and super cavity solitons”. In: *Journal of the Optical Society of America B* 32.7 (2015), pp. 1259–1266.
- [17] Miles Anderson et al. “Coexistence of multiple nonlinear states in a tristable passive Kerr resonator”. In: *Physical Review X* 7.3 (2017), p. 031031.

- [18] Aurelien Coillet et al. “Azimuthal Turing patterns, bright and dark cavity solitons in Kerr combs generated with whispering-gallery-mode resonators”. In: *IEEE Photonics Journal* 5.4 (2013), pp. 6100409–6100409.
- [19] Kensuke Ikeda. “Multiple-valued stationary state and its instability of the transmitted light by a ring cavity system”. In: *Optics Communications* 30.2 (1979), pp. 257–261.
- [20] Stéphane Coen et al. “Modeling of octave-spanning Kerr frequency combs using a generalized mean-field Lugiato–Lefever model”. In: *Optics Letters* 38.1 (2013), pp. 37–39.
- [21] Yanne K Chembo and Nan Yu. “Modal expansion approach to optical-frequency-comb generation with monolithic whispering-gallery-mode resonators”. In: *Physical Review A* 82.3 (2010), p. 033801.
- [22] Hermann Haus. *Waves and Fields in Optoelectronics*. Prentice-Hall, 1984.
- [23] Amnon Yariv. “Critical coupling and its control in optical waveguide-ring resonator systems”. In: *IEEE Photonics Technology Letters* 14.4 (2002), pp. 483–485.
- [24] Tobias Hansson and Stefan Wabnitz. “Dynamics of microresonator frequency comb generation: models and stability”. In: *Nanophotonics* 5.2 (2016), pp. 231–243.
- [25] Roland Glowinski, Stanley J Osher, and Wotao Yin. *Splitting Methods in Communication, Imaging, Science, and Engineering*. Springer, 2017.
- [26] Stéphane Coen and Miro Erkintalo. “Universal scaling laws of Kerr frequency combs”. In: *Optics Letters* 38.11 (2013), pp. 1790–1792.
- [27] Gunnar Ohlén, Sven Åberg, and Per Östborn. *Chaos*. Division of Mathematical Physics, LTH, 2007.
- [28] Marc Haelterman, Stefano Trillo, and Stefan Wabnitz. “Additive-modulation-instability ring laser in the normal dispersion regime of a fiber”. In: *Optics Letters* 17.10 (1992), pp. 745–747.
- [29] Lloyd N Trefethen. *Spectral Methods in MATLAB*. SIAM, 2000.
- [30] J Nathan Kutz. *Data-Driven Modeling & Scientific Computation: Methods for Complex Systems & Big Data*. Oxford University Press, 2013.
- [31] Michael Ekström. *Kerr Comb Simulator*. Version 1.1.0. 2022. URL: https://github.com/miceks/kerr_comb_simulator.
- [32] DV Skryabin et al. “Threshold of complexity and Arnold tongues in Kerr-ring microresonators”. In: *Physical Review A* 103.1 (2021), p. L011502.
- [33] Tobias Herr et al. “Temporal solitons in optical microresonators”. In: *Nature Photonics* 8.2 (2014), pp. 145–152.
- [34] Maxim Karpov et al. “Dynamics of soliton crystals in optical microresonators”. In: *Nature Physics* 15.10 (2019), pp. 1071–1077.
- [35] François Leo et al. “Dynamics of one-dimensional Kerr cavity solitons”. In: *Optics Express* 21.7 (2013), pp. 9180–9191.